

## Chapter 2

# Fundamentals of the Friction Stir Process

### 2.1 Overview of Macroscopic Processes During FSW

For any manufacturing process, understanding its fundamental process mechanisms is vital for its long-term growth. In this chapter, we will outline the essential characteristics of friction stir process. As pointed out in Chap. 1, unlike fusion-based joining processes, there is no perceptible melting during friction stir welding (FSW). From the operational viewpoint, a friction stir welding run can be divided into three sub-procedures or phases:

- (a) plunge and dwell,
- (b) traverse, and
- (c) retract.

At the start of the plunge phase, both the tool and the workpiece are at ambient temperature (except the region surrounding tool and workpiece interface). When the rotating friction stir tool is gradually inserted into the workpiece, the material is too cold to flow and the rubbing action creates chipping as in any machining process. The rate of insertion determines the rate of temperature rise and extent of plasticity. The process of tool insertion continues until the tool shoulder is in intimate contact with the workpiece surface. At this stage, the entire tool shoulder and pin surface contribute to the frictional heating and the force starts to drop as the metallic workpiece reaches critical temperature for plastic flow. For metals with higher melting point, the rotating tool is sometimes intentionally retained at this position for short durations so as to reach the desired temperature required for plastic flow. This is known as the dwell phase and is typically a fraction of the time required for plunge phase. Typically, the plunge stage is programmed for controlled plunge rate (i.e. vertical position controlled FSW) but it can be also done by controlling the force applied on the tool along its rotation axis (i.e. force controlled FSW). Of course, any combination of displacement and force controlled approach is possible. For a typical FSW run, the vertical force reaches a maximum value in this part of the run and this tends to be critical phase for the tool. It is important to

control the rate of heat build-up and in fact, for metals with higher melting point (e.g. steel/titanium) the plunge rate is particularly low so as to generate sufficient heat to plasticize the metal (Refer to Chap. 4 for more discussion on it).

### Box 2.1 Friction Stir Spot Welding (FSSW)

FSSW is a new spot welding technique to join overlapping workpieces and intends to replace existing techniques like resistance spot welding. The concept was first developed at Mazda Motor Corporation and Kawasaki Heavy Industry as an extension of FSW for joining Al alloys (Sakano et al. 2001). The method consists of only (a) the plunge and dwell and (c) retract stages of FSW (see Fig. 2.1). Due to absence of stage (b) of FSW (traverse stage) in FSSW, there is no concept of advancing side and retreating side, and the process is considered to be symmetrical.

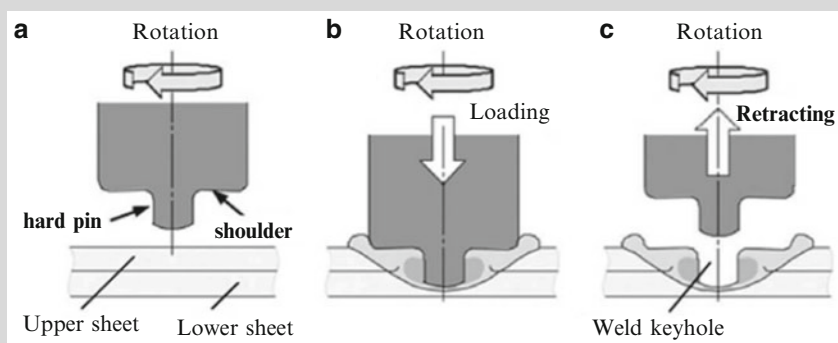


**Fig. 2.1** Two different stages (a)–(b) plunge and dwell and (c) retract in FSSW (Yang et al. 2010, reprinted with permission from Elsevier)

The FSSW procedure shown in Fig. 2.1 is known as the plunge type FSSW. Some other variants of FSSW includes (a) refill FSSW (Iwashita 2003), (b) modified refill FSSW (Allen and Arbegast 2005), (c) swing FSSW (Okamoto et al. 2005).

Once the workpiece/tool interface is sufficiently heated up, the tool is traversed along the desired direction to accomplish joining. This is the actual welding phase and can be performed under (a) displacement controlled mode (where tool position with respect to the workpiece surface is held constant) or (b) force controlled mode (normal force applied by the tool to the workpiece is held constant). There are other modes such as power control, torque control, temperature control, etc., on advanced FSW machines available these days. On completion of the joining process, the tool is finally retracted from the workpiece. In Fig. 2.2a, a schematic of the force versus time during friction stir welding is shown.

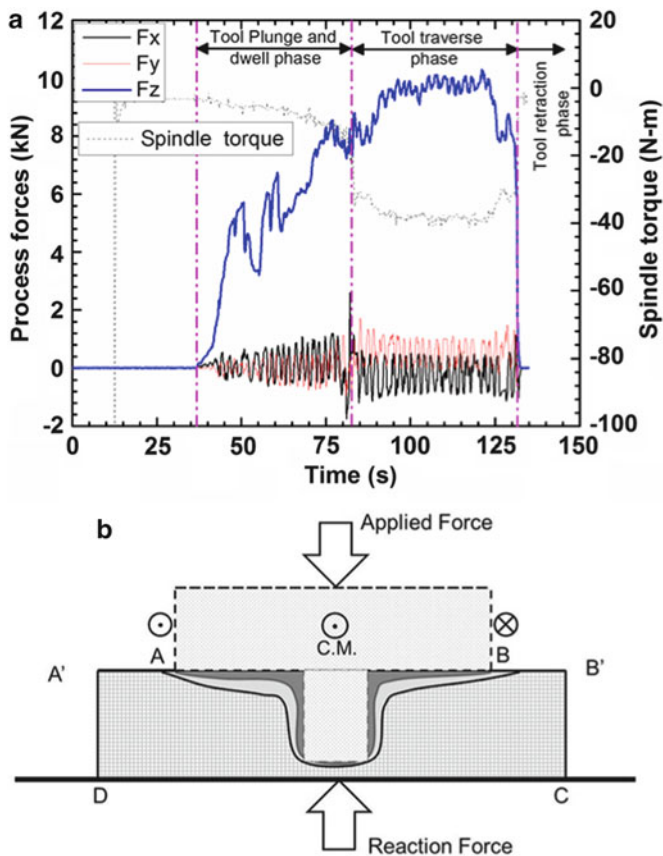


**Fig. 2.2** (a) The temporal variation of forces  $F_x$ ,  $F_y$  and  $F_z$  acting on the tool during friction stir welding. (b) Schematic transverse section of friction stir welding tool and workpiece with the tool rotating in counterclockwise direction and is moving out of the plane of the paper with the forces acting

It is instructive here to consider the physical effects occurring at the different positions of the tool/workpiece interface during the traverse phase. Thus, in Fig. 2.2b where the rotating tool shoulder presses on to the workpiece (AB/A'B' interface), frictional heat generation plasticizes the metal and pushes it downwards. Some fraction of the shoulder generated heat along with the frictional heat generated by the moving and rotating pin softens the metal adjacent to the pin. The softened metal flows around the pin, resulting in joining of the weld seam. In fact, FSW in its pseudo-steady state is conceptually quite similar to thermo-mechanical metalworking of metallic materials (Arbegast 2008). However, a key difference between FSW and elevated temperature metalworking processes is that in metal forming the workpiece is pre-heated to a critical temperature to soften the metal for subsequent deformation without any failure or cracking. But, in FSW the workpieces to be joined are at ambient temperature in the beginning and the heat

generation accomplished through mostly friction is an essential part of the process.<sup>1</sup> In contrast, in most metal forming processes, the aim is to minimize the friction so as to reduce the process energy consumption. The difference between FSW and other metal forming processes are clearly illustrated in Figs. 2.3 and 2.4.

The explanation so far has been directed towards an operational understanding of the process during FSW, and it highlights two key components in FSW process: heat generation and material flow. Figure 2.5 illustrates an overview of the principal process variables (dependent and independent) affecting material flow (deformation) and temperature distribution in FSW, and the physical effects associated with each parameter (the figure is adapted from Colligan and Mishra (2008)). The independent process variables are shown in boxes with bold lines, while the dependent variables are shown in boxes with dashed lines. The linkage between dependent and independent process variables are shown through arrows which pass through respective physical effects shown in dashed boxes in italics. Deducing the effect of independent process variables on the dependent variables through the respective physical effects is, however, more complicated. Nonetheless, simple deductions about the operational effect of different process variables can be made. For example, an increase in tool shoulder diameter and keeping all other independent process variables constant will not only impact the peak temperature and temperature distribution but also will impact the dependent variables, torque and associated power input. It gives a glimpse of the interdependencies and intricacies associated with friction stir welding. Again, increasing the spindle speed (rotation rate) or decreasing the tool travel speed is expected to increase the heat input into the weld as long as the frictional conditions remain unchanged which itself depends on the contact pressure, temperature distribution and shear stress of the workpiece. A generic flow chart of the physical effects in friction stir welding and how they affect the microstructure is shown in Fig. 2.6 (Mishra 2008). Details on how the microstructure is affected will be discussed in Chap. 3.

## 2.2 Heat Generation During Friction Stir Process

In macroscopic terms the energy flow in FSW is as below (Fig. 2.7). From Fig. 2.7, it is evident that the torque generated at the spindle and weld-arm motor can give a measure of the overall energy required for FSW (Lienert et al. 2002; Khandkar et al. 2003). Again, neglecting other losses (i.e. transmission losses), the electrical power consumed is also a good indicator of the energy trend. But, predictive modeling is practically impossible unless such direct energy measures are correlated to the actual processes in the weld zone, indicating the importance of understanding the heat generation

---

<sup>1</sup> FSW of pre-heated workpiece is also currently gaining acceptance. Predominantly a heat source like laser beam is used to pre-heat the specimen locally. This reduces the forces during FSW especially for high melting point metals like steel and copper (Kohn et al. 2002).

processes in FSW. The heat generation in FSW arises primarily from two sources, (a) friction between the tool and workpiece surfaces and (b) heat generated during plastic deformation in the bulk of the workpiece.

### Box 2.2 A Comparison of Force-Time Profiles for Various Thermo-mechanical Processes

The signature response of any manufacturing process lies in its temporal force and temperature variations. In Fig. 2.3, the reactive body force in the principal loading direction (i.e.  $F_z$ ) during FSW is compared with other manufacturing processes. The initial force peak characterizes the plunging stage, where the tool processes is more similar to machining process and the work-piece is more or less cold. However, as the heat builds up in and around the tool/work-piece vicinity, the material softens. Consequently the force drops to a more stable steady state characteristic of the actual welding stage unlike metal forming processes where the forces are intermittent type. Recent studies, however, show that the so called steady force state during FSW is in fact complicated with small periodic variations (see Fig. 2.30 in this chapter). The amplitude of these periodic variations is much smaller compared to the average load but nonetheless they carry important information about the process.

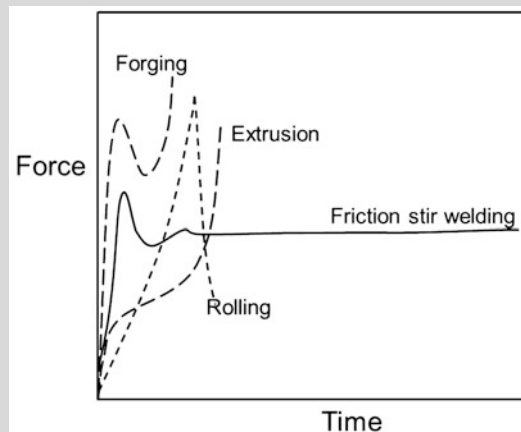


**Fig. 2.3** The force versus time curve for different metal working processes and friction stir welding process. The initial sharp increase in force with time followed by a steady state value is typical of FSW and differs significantly from the batch type metalworking operations

### Box 2.3 A Comparison of Temperature-Time Profiles for Various Thermo-mechanical Processes

Temperature variation in FSW is quite similar to other joining methods, but is distinctly different from metalworking processes. The effect of this temperature variation with time causes a significantly different effect on the workpiece during FSW. In a metalworking process the temperature variation (along with deformation) is a principal driving force in changing the microstructure of the entire workpiece. But, in FSW the localized temperature (and deformation too) gradient causes a microstructural change in a selected location (i.e. along the welded region) of the workpiece. Consequently, material property is non-uniform, unlike in metalworking processes where the property remains more or less similar throughout.

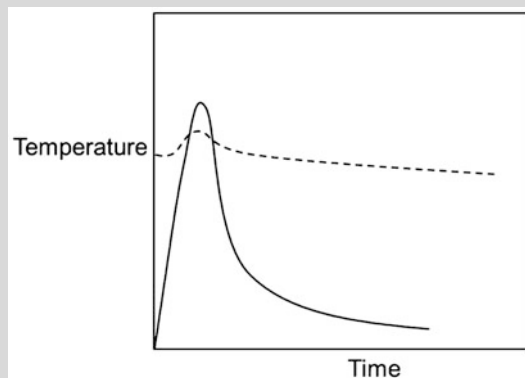


**Fig. 2.4** The sharp variation of workpiece temperature (*bold line*) with time in FSW differs significantly from the more steady variation observed in metalworking operations like rolling (*dashed line*)

#### 2.2.1 Heat Generation from Frictional Heating

Considering the frictional heat generation phenomena first: conventionally, friction between any two solids is governed by the following three empirical laws (attributed to the French scientists G. Amonton and C.D. Coulomb),

- (a) frictional force ( $F$ ) is related to the normal load ( $P$ ) by

$$F = \mu P$$

where  $\mu$  is the coefficient of static/dynamic friction. Both the static and dynamic coefficients of friction are independent of  $P$ ,

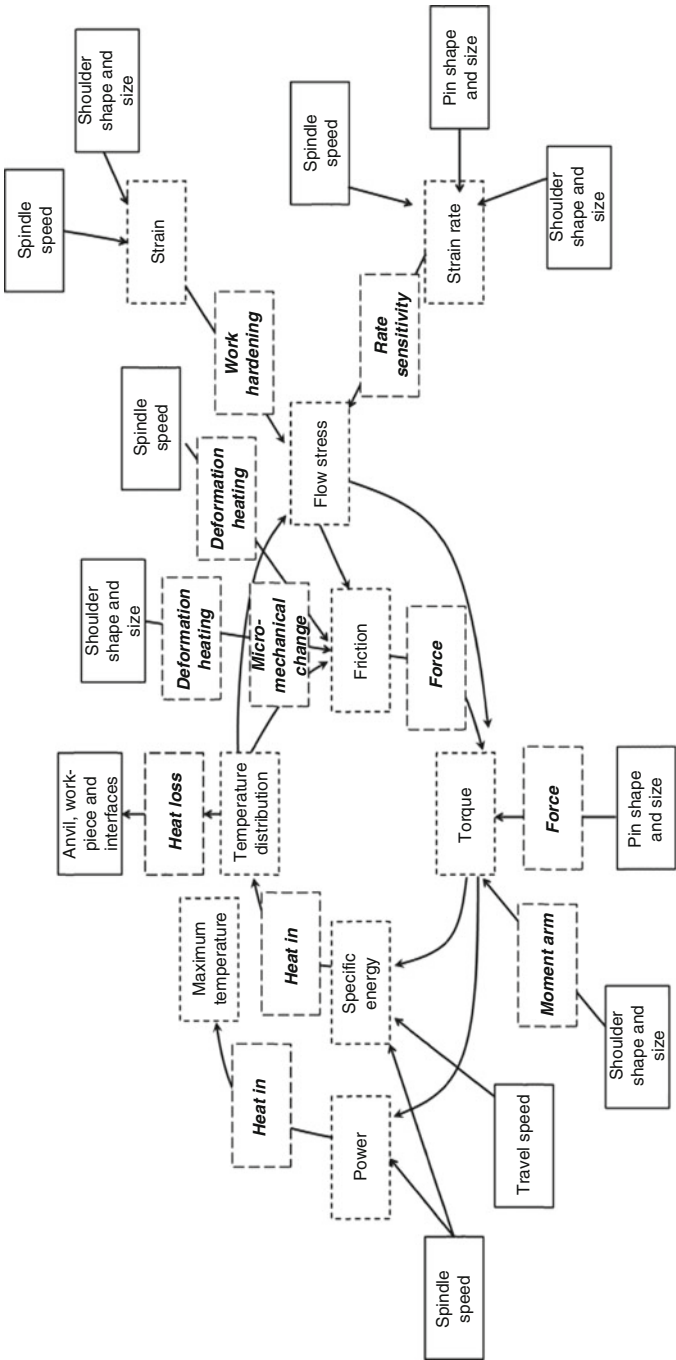


**Fig. 2.5** A schematic operational flow chart of FSW with process variables and associated physical effects (Colligan and Mishra 2008, reprinted with permission from Elsevier)

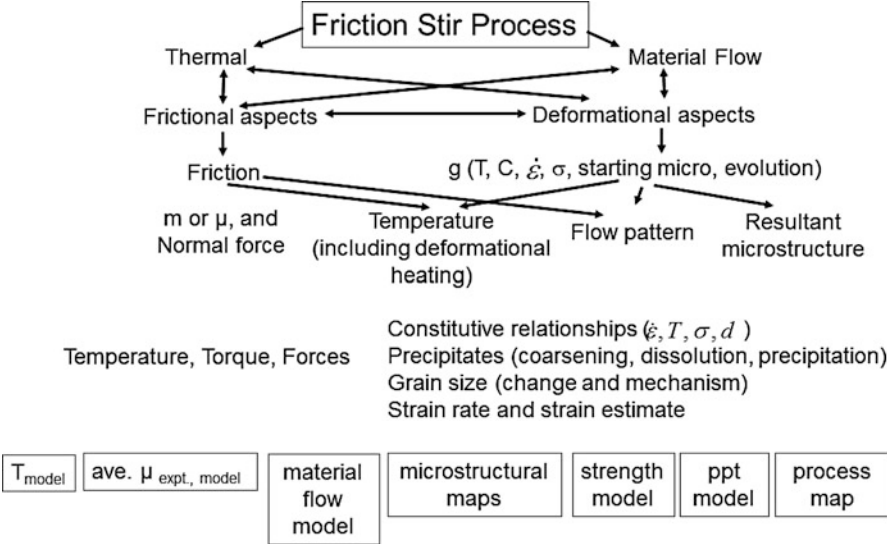


**Fig. 2.6** A summary of the physical effects in FSW and how they affect the microstructure (Mishra 2008, reprinted with permission from Elsevier)

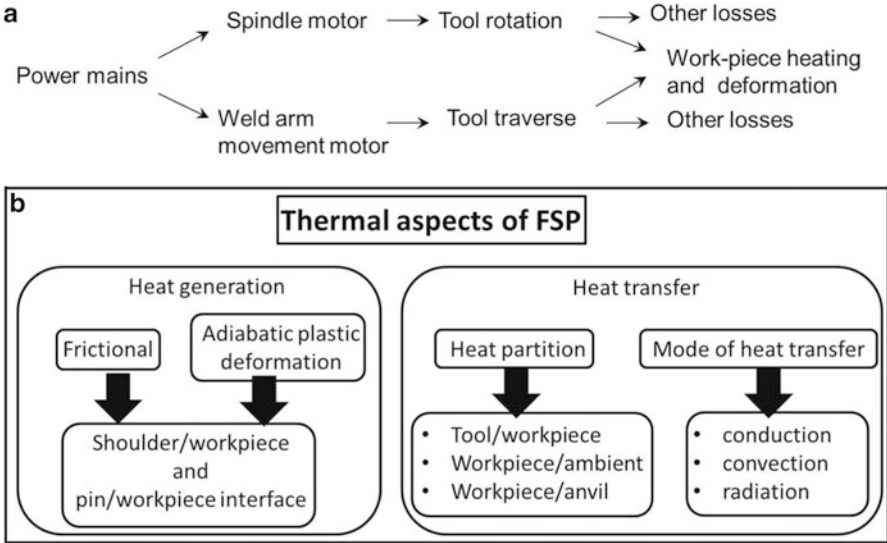


**Fig. 2.7** The flow of energy into the workpiece during FSW. (a) Energy source and its flow (b) nature of heat generation and its utilization



- (b) the coefficients of friction are independent of the macroscopic area of contact between the bodies, and
- (c) the dynamic coefficient of friction is independent of the relative velocity between the two bodies.

However, exception to the above mentioned rules are frequent and indicate the complexities involved in defining friction. According to our current understanding (Bowden and Tabor 1973), the friction between metals and/or ceramics arises due to (a) interfacial adhesion between asperities on the contacting surfaces and (b) microscopic plastic deformation during relative motion of the contacting surfaces. The frictional energy dissipated during microscopic deformations occurring at the surfaces is entirely converted to heat energy. Thus, in reality the frictional force is influenced by the physical and chemical properties of the interacting surfaces and their dependence on the load, relative velocities and temperature thereof. It is important to note that in FSW these microscopic deformations occur chiefly at the workpiece surface (the tool surface more or less is considered non-deformable although that may not be true for FSW of high temperature materials with refractory metal tools). As a consequence, the heat generated is distributed unequally between the two surfaces (i.e. tool and workpiece) (Bhushan 2002). The extent of this heat partitioning depends on the thermal conductivity, heat capacity, relative velocity and the interfacial area of the tool and workpiece.

From a theoretical viewpoint, this friction can be any of the following.

- (a) Coulomb friction

$$\tau = \mu p$$

where  $\tau$  is the shear stress,  $p$  is the pressure and  $\mu$  is the coefficient of friction.

- (b) Constant shear model

$$\tau = m\sigma_y$$

where  $\sigma_y$  is the material yield stress in shear and  $m$  is the proportionality constant with  $m$  equals to 0 for slipping condition and 1 for sticking condition. In the constant shear model, the workpiece surface in contact with the tool is considered to behave like a material with constant shear strength. The maximum shear strength possible being equal to the yield stress in shear and is equivalent to a situation where the workpiece metal sticks to the tool surface with deformation occurring by sub-surface shearing (i.e.  $m = 1$  in equation) (Dieter 1986).

In the remainder of this section, a comprehensive model of heat generation in FSW is presented. Figure 2.8 shows the schematic of a typical FSW tool, with a cylindrical pin of radius  $R_{\text{pin}}$  (i.e.  $R_{\text{probe}}$  in figure), and height  $H_{\text{pin}}$  (i.e.  $H_{\text{probe}}$  in figure) and a tool shoulder diameter  $H_{\text{shoulder}}$  (i.e.  $H_{\text{probe}}$  in figure), the surface of which is at an angle  $\alpha$  with the horizontal. The total heat generated at different portions of the tool (Schmidt and Hattel 2005) during welding is sub-divided into the following components depending on the distinct zones of the tool/work-piece interface,

**Fig. 2.8** A typical FSW tool with a conical shoulder and a cylindrical unthreaded pin [adapted from (Schmidt and Hattel 2005)]

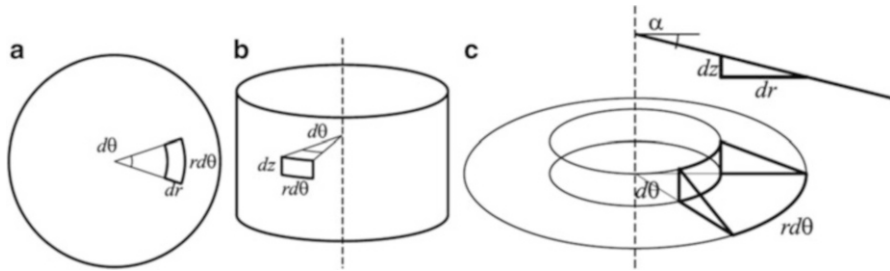
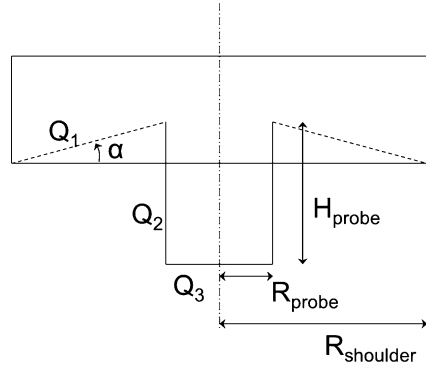


**Fig. 2.9** A schematic of the different surface segments of the tool (a) pin bottom, (b) cylindrical surface of the pin, (c) conical surface of the shoulder, and the infinitesimal segments associated with the corresponding segments (Schmidt et al. 2004, © IOP Publishing. Reproduced by permission of IOP Publishing. All rights reserved)

$Q_1$  = Heat generated at the tool shoulder,

$Q_2$  = Heat generated at the tool pin,

$Q_3$  = Heat generated at the tool pin tip.

The general expression for heat generation at each of the different zones of the tool/workpiece interface is,

$$dQ = \omega \cdot r \cdot dF$$

where  $dQ$  is the heat generated per unit time,  $dF$  is the force acting on the surface at a distance  $r$  from the tool centerline and  $\omega$  is the angular velocity of the tool.

In Fig. 2.9a the horizontal surface of the tool pin is shown. An infinitesimal segment on this surface  $dA = r d\theta dr$  is acted upon by the frictional shear stress ( $\tau_{shear}$ ) and generates an infinitesimal amount of heat given as,

$$dQ_3 = \omega \cdot r^2 \cdot \tau_{shear} \cdot d\theta \cdot dr$$

Integrating the above over the tool pin bottom area we get,

**Table 2.1** Some other approximate heat generation models used in literature

Assumptions (ref)	Heat generation equation used
1. Heat generated only at shoulder	
2. Frictional heating only, i.e. $\mu$ is the coefficient of kinetic friction (Chao and Qi 1998)	$Q = \frac{\pi\omega\mu F(R_{shoulder}^2 + R_{shoulder}R_{pin} + R_{pin}^2)}{45(R_{shoulder} + R_{pin})}$
1. The average power ( $P_{av}$ ) is related to measured torque ( $M_{total}$ ) by $P_{av} = M_{total}\omega$ (Khandkar et al. 2003)	$\dot{q}(r) = \frac{P_{av}r}{(2/3)\pi R_{shoulder}^3 + 2\pi H_{pin}R_{pin}^2}$
1. The pressure P on tool is calculated from the force (Frigaard et al. 2001)	$q_0 = \frac{4}{3}\pi^2\mu P\omega R_{shoulder}^3$

$$Q_3 = \int_{r=0}^{R_{pin}} \int_{\theta=0}^{2\pi} \omega \cdot r^2 \cdot \tau_{shear} \cdot d\theta \cdot dr$$

$$Q_3 = \frac{2}{3}\pi\tau_{shear}\omega R_{pin}^3$$

In Fig. 2.9b the cylindrical portion of the pin is shown where the infinitesimal segment  $dA = r d\theta dz$  is acted by  $\tau_{shear}$  and the heat generated is given as,

$$dQ_2 = \omega \cdot R_{pin}^2 \cdot \tau_{shear} \cdot d\theta \cdot dz$$

Integrating the above over the cylindrical surface of the pin,

$$Q_2 = \int_{\theta=0}^{2\pi} \int_{z=0}^{H_{pin}} \omega \cdot R_{pin}^2 \cdot \tau_{shear} \cdot d\theta \cdot dz$$

$$Q_2 = 2\pi\tau_{shear}R_{pin}^2\omega$$

In Fig. 2.9c the conical portion of the tool shoulder is shown where the infinitesimal segment approximated as  $dA = r d\theta (dr + dz) = r d\theta (dr + dr \tan \alpha) = r d\theta dr (1 + \tan \alpha)$ , is acted upon by the  $\tau_{shear}$  and heat generated is given as

$$dQ_1 = \omega \cdot r^2 \cdot \tau_{shear} \cdot (1 + \tan(\alpha)) \cdot dr \cdot d\theta$$

Integrating the above over the conical surface of the tool shoulder,

$$Q_1 = \int_{r=R_{pin}}^{R_{shoulder}} \int_{\theta=0}^{2\pi} \omega \cdot r^2 \cdot \tau_{shear} \cdot (1 + \tan(\alpha)) \cdot dr \cdot d\theta$$

$$= 2\pi(1 + \tan(\alpha))\tau_{shear}(R_{shoulder}^3 - R_{pin}^3)$$

In the above heat generation model, both  $\omega$  and  $\tau_{shear}$  are considered as constant. But, depending on the tool size and the tool rotation conditions these parameters can vary significantly (in terms of  $r$  and  $\theta$ ) and the heat generation expressions should be modified accordingly. Some other approximate expressions for heat generation used in literature are presented in Table 2.1. Another aspect worth

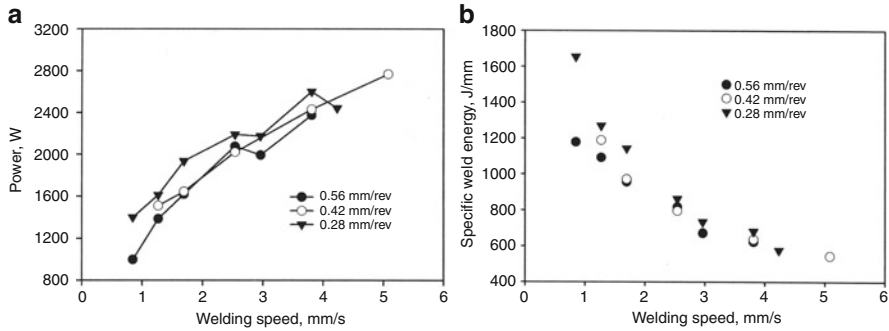


**Fig. 2.10** Plots correlating (a) Power (W) and (b) Specific weld energy (J/mm) as a function of tool traverse speed (mm/s). Here, specific weld energy is defined as the ratio of weld power to the tool traverse speed (Reynolds 2007, reprinted with permission from ASM International)

mentioning is the effect of traverse speed on the weld heat input. Although, the heat generation equations described above are independent of traverse speed, the weld heat input decreases and the power consumed increases with traverse speed increase at constant traverse speed to tool rotation rate ratios (i.e. advance per revolution (APR)) (see Fig. 2.10a). The observation is quite intuitive since in a given time now more material is processed. Also, at higher traverse speed the material ahead of the tool gets less time to preheat resulting in reduced material softening which leads to higher torque and hence higher power requirement to process the material. This aspect can be further illustrated with the help of Fig. 2.10b which gives heat input as a function of the welding speed. As the tool traverse speed increases, the heat input to the weld decreases causing less softening of the material around the tool which in turn increases the demand for higher power.

### 2.2.2 Heat Generation from Plastic Deformation

Preceding section focused on the heat generation due to friction between the tool and workpiece surface only. However, the localized plastic deformation process occurring in the bulk of the workpiece can also significantly contribute to the heat added to the weld. For example, in a uniaxial tensile test, the total energy (i.e. area under the stress-strain curve) is partially converted to heat, while the remaining is stored in the material microstructure. The amount of this plastic deformation energy which is dissipated as heat can vary between 80 and 100 % of the total input (Hodowany et al. 2000; Kapoor and Nemat-Nasser 1998). Thus, with reference to friction stir welding, the weld power input converted to plastic deformation energy in the bulk can be separated into two parts, (a) fraction stored in the microstructure, and (b) fraction converted to heat. Although, no experimental measurements of these individual fractions have been reported for FSW, the results of numerical simulations predict that the extent of heat obtained from

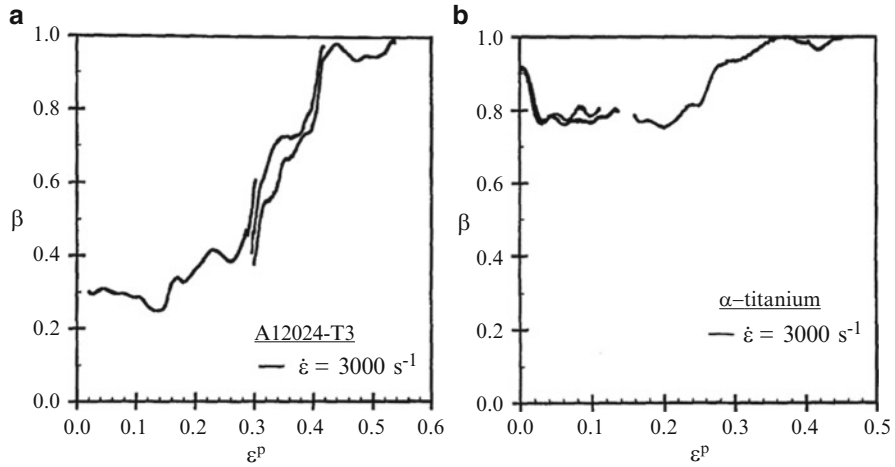


**Fig. 2.11** The fraction ( $\beta$ ) of plastic deformation energy converted to heat for (a) 2024-T3 alloy and (b)  $\alpha$ -Titanium at strain rates of  $3,000 \text{ s}^{-1}$  (Hodowany et al. 2000, reprinted with permission from Springer)

bulk plastic deformation can vary between 2 and 20 % (Russell and Shercliff 1999; Colegrove et al. 2000).

In this regard, the experimental measurements on heat dissipation using Kolsky bar and servo-hydraulic testing by Hodowany et al. (2000) of an AA 2024-T3 alloy provide some interesting insight (see Fig. 2.11). The results show that for deformation at low strain levels ( $\sim 0.4$  and below), the Al alloy could store more than 60 % of the input plastic work in its microstructure. However at higher strains, this storage ability diminished and reaches zero at strains  $> 0.5$ . The results obtained for another metal ( $\alpha$ -titanium) were also more or less similar. Additionally, this conversion of plastic deformation work to heat energy is found to be relatively insensitive to the strain rate of deformation (see Fig. 2.12). Thus, for the strain and strain rates prevailing during FSW (see Sect. 2.5), it can be safely assumed that the work done by the applied tool torque is almost totally converted to heat energy.

### 2.2.3 Heat Transfer During Friction Stir Process

The last section discussed about heat generation in FSW. But, ultimately it is the nature of heat transfer to the workpiece and tool which affects the physical property of the workpiece. In this section, we focus on the mathematical background and physical properties relevant to this heat transfer process. A schematic of the overall heat transfer process in FSW is given in Fig. 2.13 where the energy transfer destination and the principal rate controlling mechanisms associated are shown.

The governing equation for heat transfer is given as,

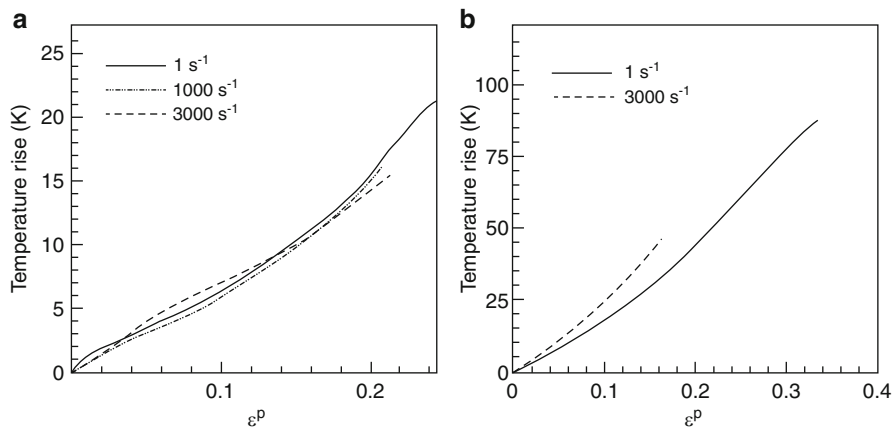


**Fig. 2.12** The rate of temperature rise during straining at different strain rates for (a) 2024-T3 alloy and (b)  $\alpha$ -Titanium (Hodowany et al. 2000, reprinted with permission from Springer)

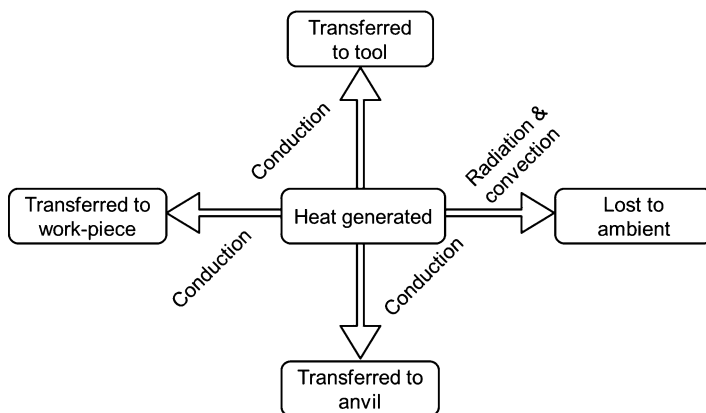


**Fig. 2.13** Schematic of the heat transfer processes occurring during friction stir process. Note that in some cases like bobbin tool the heat transferred to the anvil can be neglected. Again, heat transferred to the tool/anvil also depends on the intrinsic conductivity of anvil and tool material. Here, the convective heat transfer from workpiece to anvil/tool is assumed to be rate controlling

$$\frac{\partial}{\partial t} \rho (C_p T) = -\vec{\nabla} \cdot \rho \vec{u} (C_p T) - \vec{\nabla} \cdot (k \vec{\nabla} T) + \dot{q}$$

where  $\rho$  is the material density,  $C_p$  is the specific heat capacity,  $T$  is the temperature,  $\vec{u}$  is the velocity,  $k$  the thermal conductivity and  $\dot{q}$  is the rate of heat generation. If the convective heat transfer is neglected, the equation can be directly solved for temperature distribution by using an appropriate heat generation equation. A typical example of this approach is seen in Frigaard et al. (2001) where the heat generation equation is expressed as,

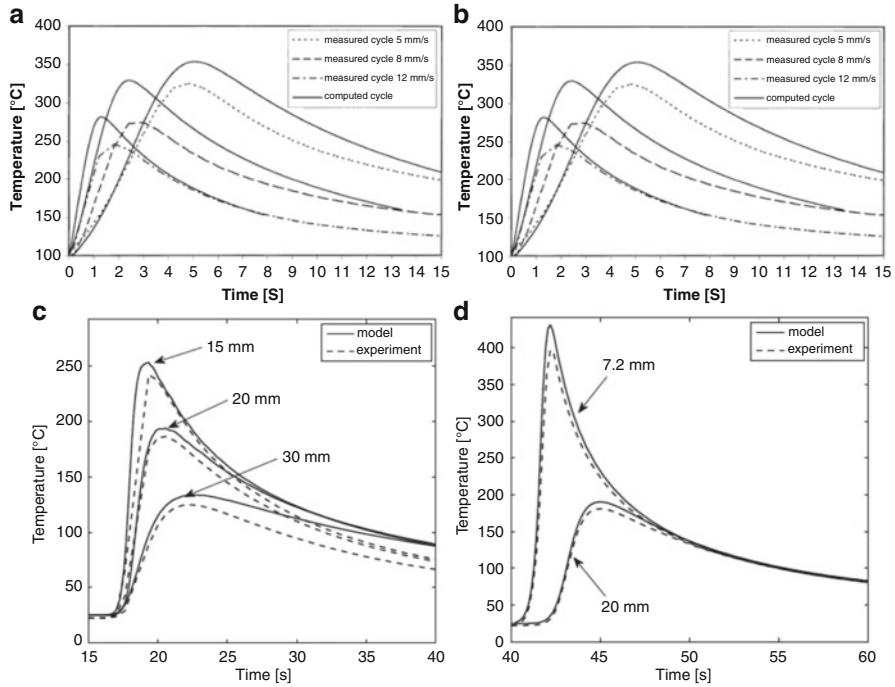


**Fig. 2.14** The measured and calculated thermal cycles in (a) AA6062, (b) AA7108 alloys where the frictional heat from shoulder/workpiece interaction is only considered (Frigaard et al. 2001, reprinted with permission from Springer). The profiles in (c) AA 6005-T6 and (d) AA 6005-T78 show the measured and calculated thermal cycles where the frictional heat was considered in its entirety (i.e.  $Q_1$ ,  $Q_2$ ,  $Q_3$ ) by measuring the torque on the tool during welding (Simar et al. 2012, reprinted with permission from Elsevier)

$$q_0 = \frac{4}{3} \pi^2 \mu P \omega R_{\text{shoulder}}^3$$

where  $P$  and  $\mu$  is assumed to be constant across the shoulder/workpiece interface and heat generation is assumed to be due to friction at shoulder/workpiece interface only (i.e.  $Q_1$ ). The heat generated due to friction at pin/workpiece ( $Q_2$ ), pin bottom/workpiece ( $Q_3$ ) and plastic deformation within workpiece bulk is ignored. A similar thermal model, neglecting the deformation aspect of FSW was solved by Simar et al. (2012) where  $q_0$  is obtained from the measured torque and rotation speed (to give power input) of the tool. In Fig. 2.14 the simulated temperatures during FSW (Frigaard et al. 2001; Simar et al. 2012) is compared with the experimental results. As expected, the error in simulated temperature arising from using pressure relationship ( $P$ ) to estimate power input is higher compared to the torque input case. Moreover, in both cases the heat transfer phenomenon at the boundaries is either neglected or is accounted for in a simplistic manner leading to errors in the overall prediction. Cho et al. (2013) measured and simulated the thermal cycle in a ferritic stainless steel using a coupled calculation where the heat transfer equation is coupled

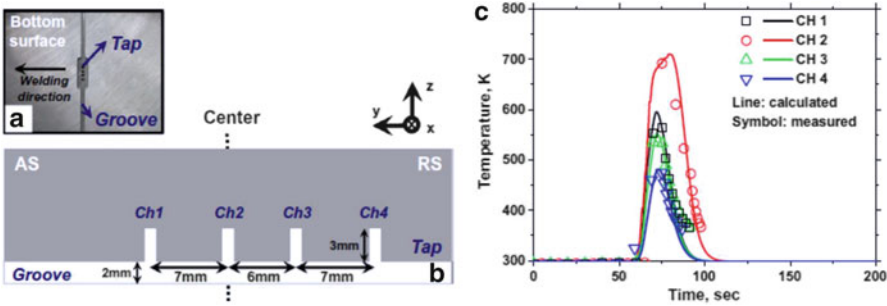


**Fig. 2.15** (a) Macrograph on bottom surface of specimen showing the actual position of four holes where thermocouples were inserted. (b) A schematic of the specimen cross-section. The direction of weld goes into the picture. (c) The measured and calculated temperature profile with time. The measured and calculated temperature profile match since the physics of the process was captured in the simulation model (Cho et al. 2013, reprinted with permission from Elsevier)

**Table 2.2** The heat transfer coefficient values used by different researchers during simulation of friction stir welding

Reference	Heat transfer coefficient (W m <sup>-2</sup> K <sup>-1</sup> )	Material welded
Schmidt and Hattel (2005)	1,000	AA2024-T3
Guerdoux and Fourment (2009)	2,000	AA 6061
Hamilton et al. (2013)	100	AA7042-T6
Nandan et al. (2006)	30	AA6061
Khandkar et al. (2006)	5,000	AA2024/AA 6061
Khandkar et al. (2006)	3,000	AISI 304L
Ulysse (2002)	0	AA 7050-T7451
Jacquin et al. (2011)	400	AA2024-T351
Aval et al. (2011)	1,000	AA 5086-O, AA 6061-T6

with the deformation calculations. Incorporation of the convective heat transfer term results in a more accurate temperature cycle prediction (Fig. 2.15).

Another significant factor influencing the temperature predictions are the boundary conditions selected which includes (a) heat loss to the anvil and (b) heat loss to the tool. Consider the different values of workpiece/anvil convective heat transfer coefficients (Table 2.2) used by researchers in current literature. It is apparent that the heat transfer coefficient value varies significantly depending on the experimental conditions. Although, in most cases a constant convective coefficient is assumed, in reality the heat transfer coefficient changes with time and temperature. This variation in heat transfer coefficient can be easily explained with relation to Fig. 2.16 where the change in initial shape of the workpiece after welding (due to residual stresses generated) is shown schematically. This change in shape depends upon the clamping conditions and workpiece characteristics causing the contact conditions to change during welding. Quite obviously the issues associated in



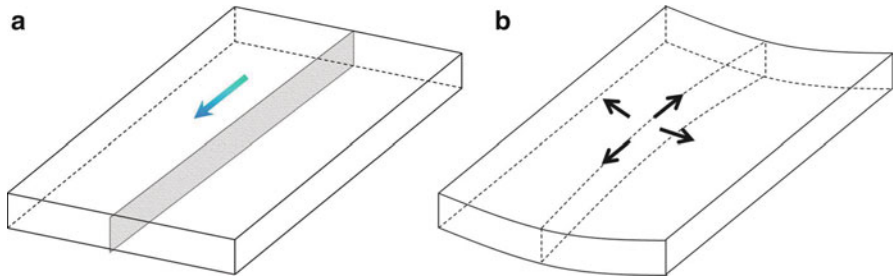


**Fig. 2.16** (a) Initial shape of the workpieces to be welded. The *shaded region* is the interface while the *arrow* shows welding direction. (b) Final shape of the workpiece due to residual stress. The deformation in shape during welding is complicated by the clamping forces

defining the convective coefficient between workpiece and anvil are subjective and difficult to define resulting in differences of heat transfer coefficient values adopted. Nevertheless, considering the average power input during FSW (ranges anywhere between ~1,000 and 3,000 W) an inappropriate choice of heat transfer coefficient can appreciably affect the simulated temperature values.

The heat transfer characteristic between workpiece and tool is significantly different from the workpiece/anvil situation. Owing to the continuous vertical pressure (during steady state welding), the workpiece/tool contact always remains intimate. Consequently, not much variation in convective heat transfer coefficient is expected. The value is also an order of magnitude larger (for example in Guerdoux and Fourment (2009) the value considered is  $50,000 \text{ W m}^{-2} \text{ K}^{-1}$ ) compared to workpiece/anvil coefficient. Thus, heat transmission to the tool is expected to be easier, although its absolute magnitude is determined by the tool/workpiece interface area which is much smaller compared to the anvil/workpiece case. Consequently, the Neumann boundary conditions can be adopted where,

$$-k \frac{dT}{dz} = -(Q_1 + Q_2 + Q_3)$$

where  $k$  is the thermal conductivity of the tool material, while  $Q_1$ ,  $Q_2$  and  $Q_3$  are as defined earlier. In the next section, material flow during FSW and its consequence on heat generation and transfer is discussed in more details.

## 2.3 Experimental Studies on Heat and Material Flow

Before, introducing the more quantitative details of friction stir welding, it is worthwhile to summarize the results from an experimental angle. A short summary of some experimental works done by different authors on deformation/material flow during friction stir welding is presented in Table 2.3. Most of these

**Table 2.3** Summary of some experimental results on deformation and material flow in friction stir welding (De et al. 2011, reprinted with permission from ASM International)

Study type (ref)	Flow pattern
Steel shots in AA6061-T6 and AA7075-T6 (Colligan 1999)	(a) Steel shots affected by shoulder deposited chaotically and moved downward. (b) Steel shots in pin front deposited continuously behind pin and moved up.
AA5454-H32 marker in AA2195-T8 (Seidel and Reynolds 2001)	(a) Material stirring occurs only at shoulder-affected zone. (b) In pin-affected zone, material moves behind its original position (c) For threaded pins, a secondary vertical flow exists.
Radioactive Ni tracer in AA2219-T8 (Nunes 2001)	(a) Metal rotated around the tool in a thin sliver just beneath shear surface ("wiping flow") in last-in/first-out mode.
Microtexture study in AA6063-T5 (Sato et al. 2001)	(a) Transverse weld section microtexture shows {111} planes as roughly parallel to pin surface. (b) The <110> directions were parallel to transverse direction. (c) Shear type of plastic flow along pin surface.
Microtexture study in AA1100, AA6061-T6, and C458 alloy (Field et al. 2001)	(a) Dominant shear direction is aligned tangent to the rotating direction. (b) Secondary shear direction along tool such that {111} planes are inclined 70° from the dominant shear direction.
Cu foil along faying surface in AA6061-T6 (Guerra et al. 2002)	(a) Advancing side material deposits behind the pin on advancing side. (b) Retreating side material stays on retreating side. (c) Vortex movement within rotational zone associated with the pin.
Microtexture study in AZ61 alloy (Park et al. 2003)	(a) Prominent basal texture (0002) of base material traced an ellipsoid surrounding the pin column (b) The effect was not noticed near the pin shoulder. (c) Onion ring structure and nugget shape associated with the elliptical trace of (0002) texture.
Al-30 vol%SiC and Al-20 vol%W markers AA7050 alloy (London et al. 2003)	(a) Upward movement of material ahead of pin. (b) Markers at advancing side distributed over a much wider region in the wake of weld compared to weld centerline. (c) Downward movement of material due to tool threads.
Microstructural studies on AA2024-T3/2524-T3 (Yang et al. 2004)	(a) Metallurgical bands (low-strain and high strain alternating bands observed on etching) form, which corresponds closely to tool marks. (b) Variation in secondary particle segregation and grain size along bands.
Microstructure studies on AA2024-T3/2524-T3 (Sutton et al. 2004)	(a) Strong correspondence between strain response and metallurgical bands. (b) High strain bands correspond to lower particle density, larger grain size. Reverse is true for lower-strain bands.

(continued)

**Table 2.3** (continued)

Study type (ref)	Flow pattern
Textural studies on AA2195-T8 alloy (Schneider and Nunes 2004)	(a) The {111} planes are aligned with the tool rotation axis. (b) Randomly oriented grains in the nugget.
Cu as marker in AA2024-T3 alloys (Schmidt et al. 2006)	(a) Average material flow velocity 0.1-0.3 times the tool rotation speed (b) Three different zones of rotation around the pin are proposed: rotation, transition, and deflection. (c) In rotational zone, material sticks to tool and undergoes multiple rotations. (No Reference Selected)

experiments trace the deformation by using marker materials embedded into the workpiece where its movement after deformation is subsequently analyzed to explain the deformation process. In fact, depending upon the type of marker used, the material flow observed can vary. Therefore, an appropriate choice of marker is critical to get a true representation, the ideal being the one which is similar in physical characteristics to the work-piece material. The results of these experiments can be broadly summarized as (Seidel and Reynolds 2001; Reynolds 2008),

- (a) deformation at the tool shoulder and workpiece interface, and
- (b) deformation at the tool pin and workpiece interface.

The nature of deformation at tool shoulder/workpiece interface is illustrated schematically in Fig. 2.17a, b, where the FSW tool transfers the marker from advancing side to the retreating side. The marker at the retreating side on the other hand moves to the advancing side. A key difference being—the circular movement of advancing side material is directed vertically downwards into the workpiece while the retreating side material is pushed vertically up towards the workpiece surface. In fact, depending upon the conditions of welding, some of the material may even be pushed out as flash on the workpiece surface.

In Fig. 2.17c, d the nature of material movement due to deformation at the tool pin/workpiece interface is shown. The marker material at the advancing side is moved approximately by the full tool circumference to reach near its original position. The marker material at the retreating side on the other hand is pushed behind the tool. As in the case of tool shoulder/workpiece interface, the movement at the pin/workpiece interface has associated vertical material movement out of its original plane.

A third deformation zone is the interface between tool pin bottom and workpiece. This deformation has some similarity to the tool shoulder/workpiece interface deformation—the difference arising from the workpiece/anvil constraint.

The marker studies by Schmidt et al. (2006), however, exhibits a more complicated material flow pattern during FSW. In this work, the authors welded an Al alloy with a copper strip (0.1 mm thick) positioned between the faying surface in two different configurations (a) faying surface parallel to the welding direction and

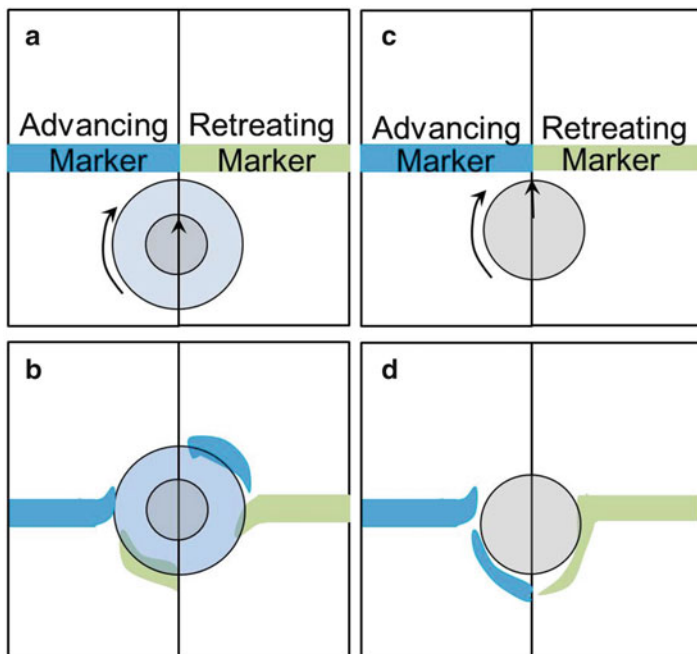


**Fig. 2.17** A schematic view of the material transport in the shoulder/workpiece interface region (a, b) and the pin/workpiece interface region (c, d)

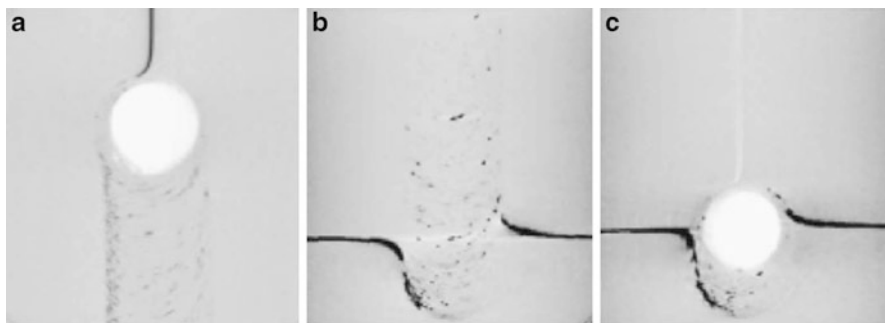








**Fig. 2.18** Displacement of marker during friction stir welding (Schmidt et al. 2006, reprinted with permission from Elsevier)

(b) perpendicular to the welding direction. The results of these experiments are presented in Fig. 2.18 where for case (a) the marker material is found to be deposited from the front side to the back side of the tool, while for case (b) the marker material is carried over several probe diameters along the direction of welding. In this particular work the linear tool movement per rotation (also known as “advance per revolution” i.e. (APR)) was 0.3 mm which is larger than the marker dimension used. In similar experiments on Al alloys by Seidel and

Reynolds (2001) using dissimilar aluminum alloy as a marker, material gets transported by a single pin diameter only. However, in this instance the APR used was 0.6 mm while the marker dimension was 1.8 mm. Similar material flow studies by Askari et al. (2001) for an APR of 0.3 mm using SiC markers of 0.8 mm diameter, resulted in displacement of the marker by more than one pin revolution. Thus, depending on the test setup the marker experiments can show different results and is therefore open to multiple interpretations.

**Box 2.4    Material Flow During FSSW**

Different methods including tracer, dissimilar weld and crystallographic texture variation has been used to investigate material flow in FSSW. Broadly, the material flow in FSSW is considered to be an effect of three different motions: (1) material flow under the shoulder towards the root of the probe along tool surface, (2) flow of material along the pin surface towards the pin bottom, and (3) upward flow of material from the pin bottom towards the shoulder away from pin surface which merges with flow (1)/(2) (Su et al. 2006, 2007; Yang et al. 2010). This is clearly observed in the work of Tozaki et al. where the authors spot welded two different 6000 series alloy sheets (different Cu contents) and obtained its macrostructure (see Fig. 2.19). The effect of different tool probe height and dwell time on the material flow and appearance of the stir zone is also clearly visible.

Tool holding time		0.2 sec	3 sec
Probe length	2.4 mm		
	3.1 mm		
	3.7 mm		

**Fig. 2.19** The flow of material during FSSW for different probe length and dwell time. Note that the ingress of lower material (*dark etched region*) towards the probe root can be considered to be a proof of motion (1). The upward movement of lower material can be considered to be a proof of motion (3). The presence of upper material (*light etched region*) below the joint line of two materials can be considered to be a proof of motion (2) (Tozaki et al. 2007, reprinted with permission from Elsevier)

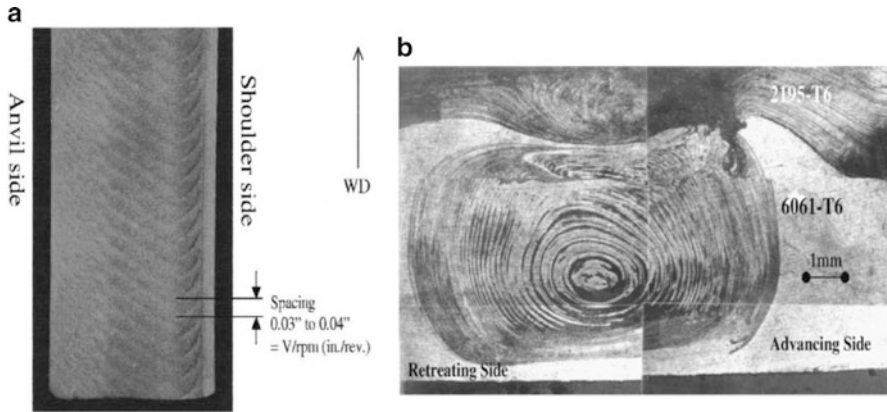


**Fig. 2.20** The onion rings/band patterns as observed on the (a) lateral section (Schneider and Nunes 2004, reprinted with permission from Springer) and (b) transverse section (Guerra et al. 2002, reprinted with permission from Elsevier) of a friction stir weld

So far, we have broadly identified the different deformation zones in a friction stir weld. But on a finer scale this deformation is associated with a more intricate feature generally known as the “metallurgical band” or “onion rings” as shown in Fig. 2.20 and is unique to friction stir welding and related processes. Macroscopically, they are observed as a repetitive pattern on the transverse and lateral section of the weld and arise due to a rhythmic variation in grain size, second phase distribution and/or grain orientation (i.e. texture). The patterns repeat at an interval (as observed in lateral section) equal to the linear distance travelled by the tool during each revolution. Although, the origin of this pattern is still unsolved, recent research on the topic suggests that it is associated with the oscillation of the tool rotation axis about its linear travel axis. More about this will be discussed in a later section of this chapter.

So far we discussed the nature of deformation, but it is worth pointing out that this is intimately connected to the thermal cycle during FSW. It is this thermal cycle which determines the nature of metal flow and depends on

- (a) heat generated due to friction between tool shoulder/pin and the workpiece, and
- (b) some additional heat produced by the plastic working of the metal already softened by the frictional heat generated.

Assuming a Coulomb friction model, the shear stress between tool and workpiece can be estimated from the measured spindle torque and the surface area of the tool/workpiece interface. The variable  $p$  is obtained from the force perpendicular to the workpiece and the tool shoulder diameter. For the constant shear model, one needs to know the strain and temperature conditions in the welded region and the yield stress of the materials for corresponding condition. This requires a thorough knowledge about the constitutive behavior of the metal, more of which will be discussed in a later part of this chapter. In fact, majority of the numerical simulations reported in literature assume a constant shear model with sticking friction condition (i.e.  $m \sim 1$ ). Measurements in FSW based on the Coulomb’s law of

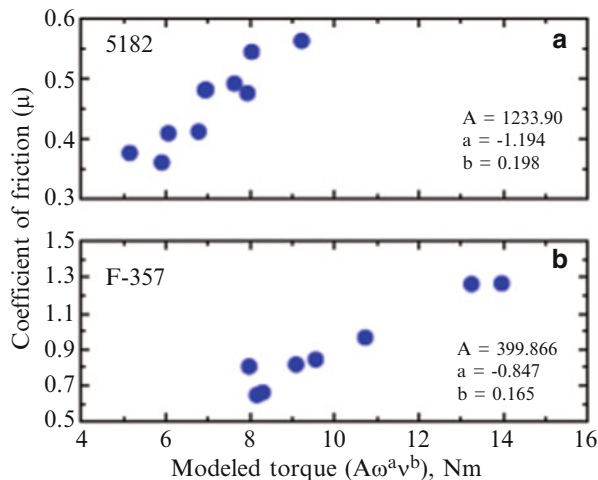


**Fig. 2.21** The variation of Coulomb's friction coefficient in FSW measured for two different Al alloys, (a) AA 5182 and (b) F-357 (Colligan and Mishra 2008, reprinted with permission from Elsevier)

friction show that  $\mu$  is a function of the material welded and shear stress itself and can vary anywhere between 0.3 and 1.5 (Fig. 2.21). In fact, based on the premise that  $\tau$  is relatively independent of  $p$ , (for all other conditions remaining same) it is argued that the constant shear model is more appropriate. At this point of time, our understanding of the frictional conditions in FSW is, however, less than complete.

### Box 2.5 Relation Between Friction and Yield Stress

In metal-working conditions the friction between workpiece and tooling is an important concern and both Coulomb's coefficient and constant shear model approaches have been used. The pressure ' $p$ ' in Coulomb's model can equal the uniaxial yield stress or be even higher. However, the shear stress ' $\tau$ ' cannot exceed the yield stress in shear. This shear yield stress is sometimes related to uniaxial yield stress using Von-Mises' or Tresca criterion.

Any discussion on friction is incomplete without some mention of the temperature ranges during FSW. Direct contact type measurement of temperature in friction stir welded zone is difficult since the thermocouple tends to disintegrate during the deformation.<sup>2</sup> Therefore, most of the direct measurements reported in literature

<sup>2</sup> Direct temperature measurements reported by Rule and Lippold (2013) for Ni-based alloys show peak temperatures in the range of  $\sim 1,100$  °C. These reports are yet to be verified by other researchers. Nugget zone temperature in the range of 450–530 °C are recorded for AA 7075 alloy friction stir spot welds using thermocouples inserted in tool (Gerlich et al. 2006). These welds are however done at tool rotation speeds of 1,000–3,000 rpm with dwell period varying from 1 to 4 s.

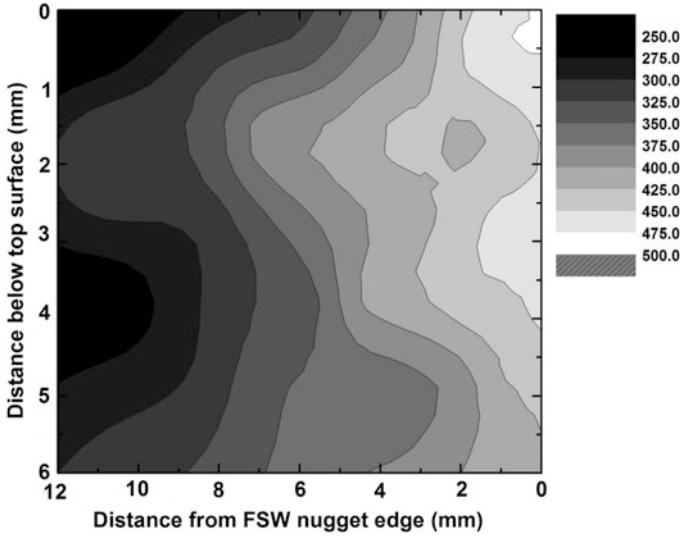


**Fig. 2.22** Contour map showing the variation in temperature from *top* to the *bottom* of the workpiece at a region adjacent to the nugget region as measured using thermocouple [adapted from (Mahoney et al. 1998)]

are away from the actual weld region (Fig. 2.22). Non-contact type measurements of the weld surface using infrared thermal imaging systems are however available. The temporal variation in both cases shows a similar trend in that the measured temperatures are below the melting point but above the recrystallization temperature of the workpiece metal. However, the situation can be quite different during dissimilar metal joining where melting can occur depending on the processing conditions (Firouzdor and Kou 2010) and metallurgical interactions.

## 2.4 Material Flow Basics

Section 2.3 presented the principal characteristics of material flow during FSW. In this section, the theoretical frameworks and its implications thereof with regards to the nature of deformation is discussed. Broadly, these explanations are based on (a) numerical or (b) analytical modeling and are centered on the plastic deformation or the fluid flow approaches. The numerical models are predominantly based on finite element/volume methods while the analytical investigations utilize fluid dynamics except on rare occasions where plastic deformation approach is used (Arbegasht 2008). The use of fluid flow approach is merely for the convenience of modeling and does not imply any affirmation of melt formation during FSW. In fact, the absence of (a) typical solidification microstructure (except in some cases of dissimilar metal joining) and (b) the nature of shear stress during FSW confirm the generally accepted solid state deformation model in FSW.



### Box 2.6 How Fluid Differs from a Solid

When a shearing force is applied on a solid the shear stress measured is proportional to the strain generated. On the other hand, a fluid flows under the slightest shear stress, i.e. continual application of the stress can result in an infinite strain. Thus, for a fluid, the shear stress is dependent on shear strain rate, i.e.

$$\tau = \mu \frac{dv}{dy}$$

where  $\mu$  is the coefficient of viscosity and  $\frac{dv}{dy}$  is the strain rate. For crystalline solids at high temperature, application of stress leads to creep deformation, when strain accumulates with time. The shear stress also varies with strain rate at high temperatures. But, all such deformations are a consequence of dislocation and point defect interaction (except at very high strain rates  $\sim > 10^7$  when adiabatic shear bands form).

Depending upon the deformation conditions the constitutive behavior of metals can exhibit a trend where the strain is independent of the flow stress. Thus, during dynamic recovery of certain metals (more is discussed in Chap. 3) the strain becomes virtually independent of stress. In such instances, the non-Newtonian fluid flow approach has been successfully applied to understand deformation behavior in FSW.

This fluid flow based treatments are based on the premise that materials behave like a incompressible fluid, and rests on the following principles,

- (a) conservation of mass (i.e. continuity equation),
- (b) conservation of momentum, and
- (c) conservation of energy (coupled with (a) and (b) or standalone).

For a non-reactive fluid, with different chemical species this mass conservation in three dimensions is expressed as,

$$\frac{\partial(\rho u X_i)}{\partial x} + \frac{\partial(\rho v X_i)}{\partial y} + \frac{\partial(\rho w X_i)}{\partial z} = 0$$

where,  $u$ ,  $v$  and  $w$  are the components of the fluid velocity,  $\mathbf{V}$  in  $x$ ,  $y$  and  $z$  directions,  $\rho$  is the density of the fluid and  $X_i$  is the mass fraction of species ' $i$ '. In addition to the above convective mass flow, presence of diffusion will result in consideration of diffusive fluxes,

$$\mathbf{J}_i = -D_i \nabla X_i$$

and the mass conservation equation becomes,

$$\frac{\partial(\rho u X_i)}{\partial x} + \frac{\partial(\rho v X_i)}{\partial y} + \frac{\partial(\rho w X_i)}{\partial z} + \nabla \cdot \mathbf{J}_i = 0$$

For a reactive fluid, with different chemical species, the mass conservation equation assumes a more general form as below,

$$\frac{\partial(\rho X_i)}{\partial t} + \frac{\partial(\rho u X_i)}{\partial x} + \frac{\partial(\rho v X_i)}{\partial y} + \frac{\partial(\rho w X_i)}{\partial z} + \nabla \cdot \mathbf{J}_i = A_i$$

where  $\frac{\partial(\rho X_i)}{\partial t}$  is the rate of change of mass of the species,  $X_i$  per unit volume and  $A_i$  is the rate of accumulation of species  $X_i$  per unit volume. At this point, it is worth mentioning that kinematics of fluid motion adopts either of the approaches,

- (a) Eulerian
- (b) Lagrangian

In the Eulerian approach, the change in properties of the fluid at a particular point of the space is recorded as a function of time. Thus, in this approach a concentration change is expressed as  $\partial X_i / \partial t|_{x,y,z}$ . In the Lagrangian approach, the path of each individual fluid particles are tracked and the temporal change in property (e.g.: concentration) are recorded for the corresponding position with time. The change in concentration with time in Lagrangian approach is represented as  $DX_i/Dt$  and is known as material derivative where,

$$\begin{aligned} \frac{DX_i}{Dt} &= \frac{\partial X_i}{\partial t} + u \frac{\partial X_i}{\partial x} + v \frac{\partial X_i}{\partial y} + w \frac{\partial X_i}{\partial z} \\ \text{Or, } \frac{DX_i}{Dt} &= \frac{\partial X_i}{\partial t} + \vec{v} \cdot \nabla X_i \\ \text{Or, } \frac{DV}{Dt} &= \frac{\partial V}{\partial t} \Big|_{x,y,z} + (\nabla \cdot \mathbf{V}) \mathbf{V} \end{aligned}$$

The general conservation of momentum equation is given as (Bird et al. 2007),

$$\frac{\partial}{\partial t} \rho \vec{v} = - \left[ \nabla \cdot \rho \vec{v} \vec{v} \right] - \nabla p - \left[ \nabla \cdot \vec{\tau} \right] + \rho \vec{g}$$

For constant  $\rho$  and  $\mu$ , expressing  $\vec{\tau}$  in terms of Newton's law of viscosity, we get the Navier-Stoke's equation. The material flow during FSW, however, does not follow the Newtonian behavior and choice of proper constitutive behavior is, therefore, critical to a realistic simulation. The typical boundary conditions used during material flow calculations are shown in the Fig. 2.23.

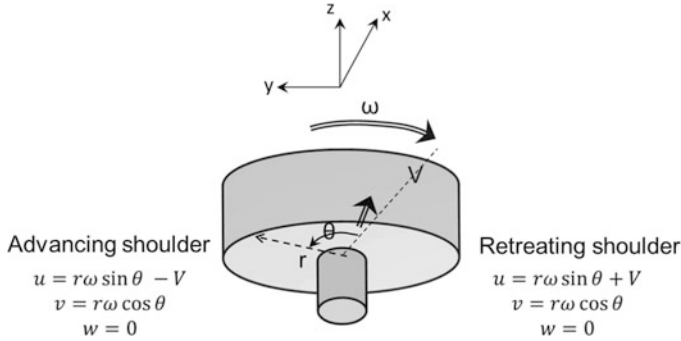


**Fig. 2.23** A typical material flow boundary condition adopted at the tool/workpiece interface for fluid flow based simulations (the tool traverse direction is out of the paper towards the reader)

The boundary conditions along the vertical pin surface depends on the pin type (e.g., threaded or smooth) and will be similar to that along the shoulders, except for the velocity along  $z$  direction, which can be approximated as,

$$w = t.p. \times \left( \frac{\omega}{2\pi} \right)$$

where,  $t.p.$  is the thread pitch of the tool. It is apt to mention here that even without the threading some amount of vertical material movement is expected.

### Student Exercise

Explain why FSW will have vertical movement even with cylindrical, unthreaded pin.

The strain rate during such fluid flow treatment is calculated based on the effective strain rate ( $\dot{\epsilon}$ ) and is given as,

$$\dot{\epsilon} = \left( \frac{2}{3} \epsilon_{ij} \epsilon_{ij} \right)^{1/2}$$

where  $(i,j) = x, y, z$  and  $\epsilon_{ij}$  is the strain which is expressed as below,

$$\begin{aligned} \epsilon_{xy} &= \frac{1}{2} \left( \frac{\partial v}{\partial x} + \frac{\partial u}{\partial y} \right) \\ \epsilon_{xx} &= \frac{\partial u}{\partial x} \text{ etc.} \end{aligned}$$

The effective stress ( $\sigma_e$ ) is calculated from the material constitutive equation and can have the following typical form,

$$\sigma_e = \frac{1}{\alpha} \sinh^{-1} \left( \left( \frac{Z}{A} \right)^{1/n} \right)$$

where

$$Z = \dot{\epsilon} \exp \left( -\frac{Q}{RT} \right)$$

$Z$  is known as the Zener-Hollomon parameter,  $Q$  is the activation energy (or fundamentally more appropriately expressed as temperature dependence),  $\alpha$  and  $A$  are material constants. The coefficient of viscosity for the material is calculated based on the effective strain rate and effective stress using the following equation (Zienkiewicz et al. 2005),

$$\mu = \frac{\sigma_e}{3\dot{\epsilon}}.$$

It should be noted that the stress is not directly calculated in the fluid flow approach and the residual stress in the weld cannot be estimated directly by this method. Another, disadvantage of the fluid flow based method is its inability to predict discontinuities (uninterrupted material flow is enforced by the continuity equation), in contrast to practical welds where discontinuities/defects do happen depending upon the friction stir process parameters. The simulation of FSW using the Lagrangian approach holds an edge over the Eulerian approach in this aspect, although its numerical stability is poor compared to the fluid flow based methods. The excessive mesh deformation occurring during FSW simulation (in FEA methods) makes the Lagrangian formulation more difficult to implement. The ALE (arbitrary Lagrangian-Eulerian) technique is a hybrid numerical method where the mesh deformation issue faced by Lagrangian method is overcome by artificially moving the boundaries (i.e. nodes) by some prescribed velocity. The convective terms in the equation are adjusted with reference to this velocity. The ALE method is suitable for analyzing large scale deformations (as in FSW) occurring over a short time period which makes it essential to use mass scaling techniques when longer time durations are required to be investigated (as during steady state welding period). The essential details of the ALE technique are available in reference (Belytchko et al. 1982; van der Lugt and Huetnik 1986).

### 2.4.1 Flow Zones Around the Tool Pin

The experiments on material flow (see Table 2.3) and the numerical simulation results indicate that material flow in the region adjacent to pin occurs primarily

by shear and can be divided into following zones (Schmidt et al. 2006; Guerra et al. 2002),

- (a) rotation zone, and
- (b) transition zone and deflection zone.

### Box 2.7 Concept of Streamlines in Fluid Flow

A simpler way to understand the material flow is to use the concept of streamlines, which are just a family of curves representing the instantaneous velocity of the fluid. Thus, for an Eulerian description, it connects all the points which have the same velocity at the given time instance. For steady state flow the streamlines are fixed in space and unchanged with time while in unsteady case the streamlines continually changes with time. If, the flow rate between two adjacent streamlines is  $d\psi$ , then using the continuity concept we get,

$$d\psi = -vdx + udy$$

Again considering flow rate to be a function of position i.e.  $\psi = \psi(x, y)$ , we get,

$$u = \frac{\partial \psi}{\partial y}, v = -\frac{\partial \psi}{\partial x}$$

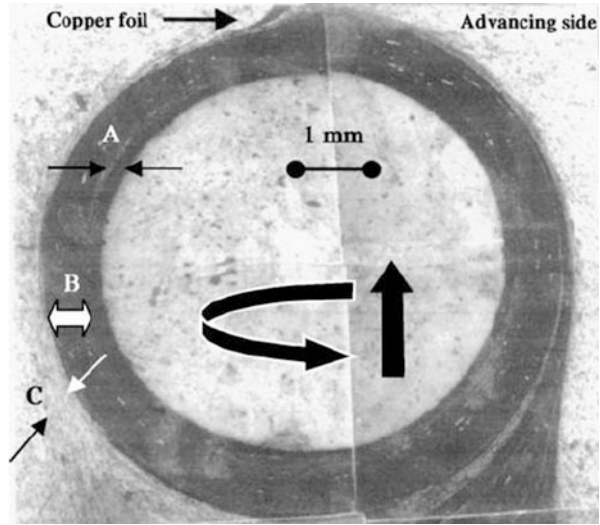
The variable  $\psi$  is known as the stream function. Knowing the stream function of a flow, the velocity at any point can be calculated.

The rotation zone is positioned immediate to the tool surface where material movement is a combination of transverse and longitudinal displacement (w.r.t workpiece) as well as angular displacement with respect to the tool axis. The transition zone comprises of the sheared layer situated in between the rotation zone and the matrix/shear layer border. Schmidt et al. (2006) defined an additional deflection zone surrounding the transition zone which is characterized by low deformation. The experiments of Guerra et al. (2002) does indeed indicate the presence of two zones, which they characterized as (a) rotation zone and (b) transition zone (see Fig. 2.24). However, a comprehensive understanding about the nature of flow in and around the pin and shoulder of the tool is still lacking.

## 2.4.2 Strain and Strain Rate During FSW

Due to the complex nature of material flow very limited experimental studies exists on strain and strain rate in FSW. Chen and Cui (2009) estimated the strain and strain rate in an A356 (Al-7Si-0.3 Mg) cast alloy using pin-breaking (modified stop

**Fig. 2.24** The region *A* indicates the gap between tool and workpiece. The region *B* is the rotation zone, while region *C* is known as the transition zone. The *central white region* shows the position of the pin (Guerra et al. 2002, reprinted with permission from Elsevier)



action) technique. In this work, the shape of a deformed dendrite is traced in the deflection zone and strain is calculated at several points along the trace of the dendrite till the point it entered the shear zone. To calculate the strain an X–Y grid is superimposed on the deformed material and new X and Y position of each point is recorded. The strain is calculated as,

$$\varepsilon = \ln\left(\frac{l}{l_o}\right) = \ln\left(\frac{\sqrt{\Delta x^2 + \Delta y^2}}{\Delta y}\right)$$

The FSW strain rate is estimated by the use of calculated strain and tool traverse speed ( $v$ ). The expression used to calculate strain rate is given as

$$\dot{\varepsilon} = \frac{\Delta \varepsilon}{\Delta t} = \frac{\Delta \varepsilon}{\Delta y} \times \frac{\Delta y}{\Delta t} = \frac{\Delta \varepsilon}{\Delta y} \times v$$

The results from their study are shown in Fig. 2.25. There is a continuous rise in strain and strain rate as it approaches the shear zone with a maximum strain of 3.5 (Fig. 2.25a) at the shear zone boundary. The maximum shear strain rate value at this point is  $85 \text{ s}^{-1}$  (Fig. 2.25b). Here, it should be noted that these workers used the deformed material ahead of pin (leading side) to estimate strain and strain rate. In a similar approach, Jata and Semiatin (2000) investigated the grains sheared in the thermo-mechanically affected zone (TMAZ), and an effective strain rate of  $10 \text{ s}^{-1}$  was reported. Frigaard et al. (2001) estimated the strain rate as  $1\text{--}20 \text{ s}^{-1}$  in aluminum alloys (AA6082-T6 and AA7108-T79) from the relationship between

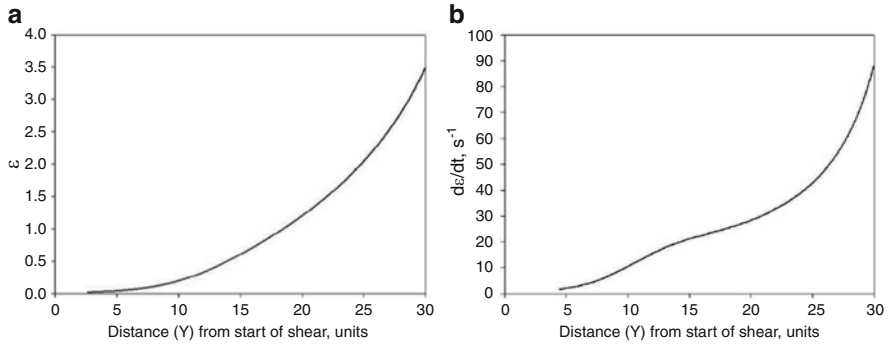


**Fig. 2.25** Variation of (a) estimated strain and (b) strain rate based on the study of deformation of dendrite trunk trace (Chen and Cui 2009, © IOP Publishing. Reproduced by permission of IOP Publishing. All rights reserved)

subgrain size ( $w$ ) and Zener-Hollomon parameter ( $Z$ ), using temperatures obtained from heat transfer calculations. The relationship between  $w$  and  $Z$  given as

$$w = [-0.60 + 0.08 \log Z]^{-1}$$

where

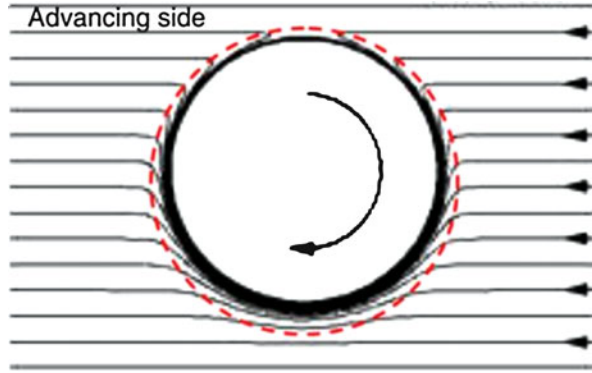
$$Z = \dot{\epsilon} \exp\left(\frac{18772}{T_p}\right)$$

and  $T_p$  is the peak temperature attained during FSW.

In another study, Mukherjee and Ghosh (2010) used AA5083 plates containing 290  $\mu\text{m}$  thick AA5457 foil in parallel and perpendicular orientations to the tool traverse direction. Using the deformation information of the foil the strain in FSW was estimated to be 4.6. Masaki et al. (2008a, b) estimated the strain rate in AA1050 during FSW using process simulation where AA1050 samples are subjected to plane strain compression at different strain rates (1, 10, and 32  $s^{-1}$ ). This is followed by cooling of the deformed material to simulate the cooling cycle during FSW. The grain size obtained from plane strain compression experiments are compared to that obtained during welding and based on grain size equality it is concluded that the strain rate in FSW is 1.8  $s^{-1}$ . It is worth mentioning here that validity of such analysis depends on the accuracy of the temperature measured during FSW process. Some uncertainty in strain rate estimate can also arise due to approximations in the grain size estimate since observed grain sizes in FSW microstructure are usually a result of recrystallization and grain growth. Process simulation done by Chang et al. (2004) assumes a torsion type deformation and the strain rate is calculated as

$$\dot{\epsilon} = \frac{R_m \cdot 2\pi r_e}{L_e}$$

**Fig. 2.26** The streamline flow field from 2D computational fluid dynamics model representing material flow around a tool pin (Reynolds 2008, reprinted with permission from Elsevier)



where  $R_m$ ,  $r_e$ , and  $L_e$  are average material flow rate, radius, and depth of the dynamically recrystallized zone. The strain rate calculated varies from 5 to  $50 \text{ s}^{-1}$  for tool rotational rates of 180–1,800 rpm.

Long et al. (2007) and Reynolds (2008) used computational fluid dynamics simulation to model the material deformation as a 2D flow field around the tool pin (Fig. 2.26). The tool rotation is considered to be counterclockwise traversing from left to right while the dashed circle around the pin represents the shear zone boundary.

In this model, it is assumed that each streamline intersecting pin on the leading side of the tool gets transported to the trailing side to a position equal to the respective chord length (directly opposite to its original position). Based on this assumption, Long et al. (2007) came up with the following expression to calculate strain at different points of the FSW shear zone

$$\varepsilon = \ln\left(\frac{l}{APR}\right) + \left| \ln\left(\frac{APR}{l}\right) \right|$$

where

$$l = 2r \cos^{-1}\left(\frac{r-x}{r}\right)$$

Here,  $l$  is the maximum stretched length of a material in the shear zone of initial length equal to  $APR$ ,  $r$  and  $x$  are the radius of pin and distance of the streamline from the retreating side of the tool, respectively. The estimated strain distribution in the processed zone for an  $APR$  of 0.5 mm/rev and a pin diameter of 10 mm is presented in Fig. 2.27 where strain on the retreating side is observed to be zero and reaches a maximum ( $\sim 8$ ) on the advancing side. The finding corresponds to the experimental observation where shear zone sharply transitions from the base to the advancing side of the weld compared to the gradual transition on the retreating side.

The calculated average strain and strain rate variation with tool rotation is presented in Fig. 2.28 where both the parameters increases with increase in tool rotational rate.



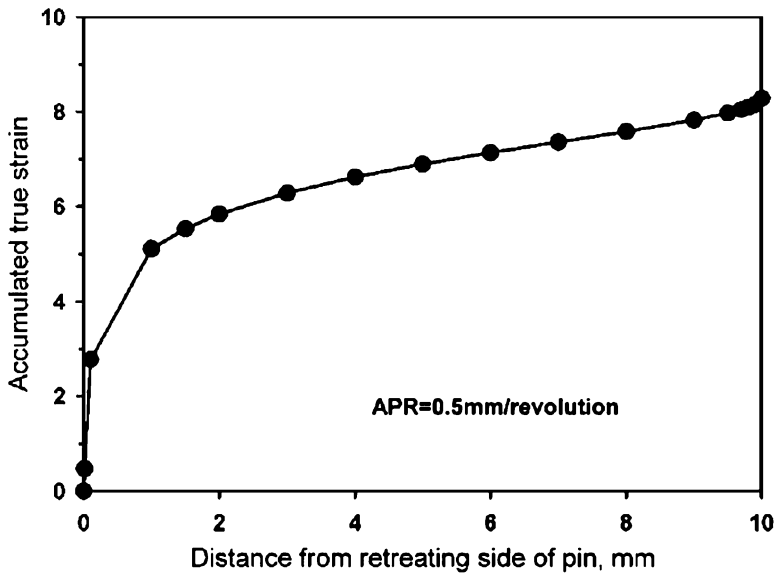


Fig. 2.27 Variation in strain from retreating side to advancing side for APR = 0.5 mm/rev and a tool pin diameter = 10 mm (Long et al. 2007, reprinted with permission from Maney Publishing)

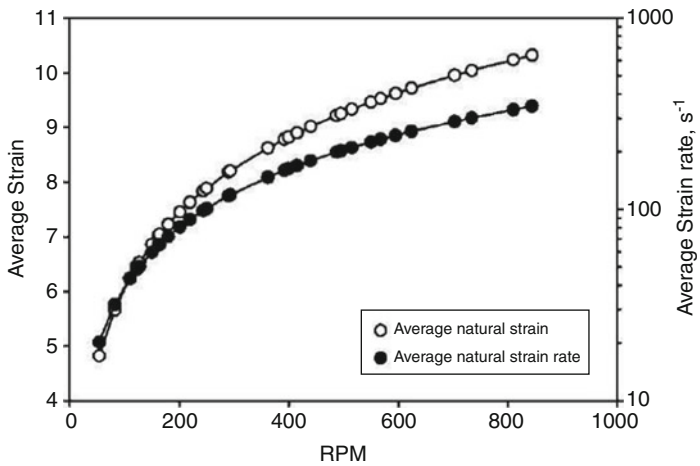
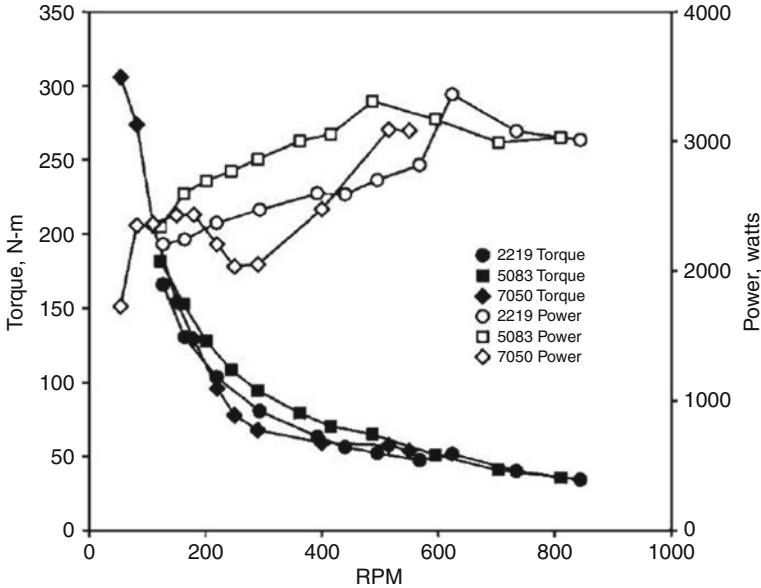


Fig. 2.28 Variation of average strain and strain rate as a function of tool rotational rate (Long et al. 2007, reprinted with permission from Maney Publishing)



**Fig. 2.29** The variation in torque during with tool rotation rate during FSW of three different Al alloys. The traverse speed remained constant (Long et al. 2007, reprinted with permission from Maney Publishing)

The continuum based FEM simulation by Buffa et al. (2006a, b) on the other hand predicts the strain and strain rate to be of the order of  $5\text{--}7$  and  $4\text{--}8\text{ s}^{-1}$ , respectively. The fluid dynamics based simulation by Nandan et al. (2006) predict a varying strain rate with a value of  $\sim 100\text{ s}^{-1}$  near the shoulder and  $30\text{ s}^{-1}$  at a distance  $4\text{ mm}$  below the surface.

It may be mentioned that all calculations from simulation and experimental estimates involve simplifications and/or assumptions arising due to lack of complete understanding of the process. Hence, while the actual strain and strain rates are expected to be different from the values reported here, in general, the magnitude of strain and strain rates are expected to be in the range of values covered here.

### 2.4.3 Forces During FSW

The forces and torque generated during joining can give important insight into the nature of ongoing process in FSW. In this regard, the experimental work of Long et al. (2007) on three different Al alloys (AA2219, AA5083 and AA7050) using a force controlled FSW deserves special mention. Some of the key findings of this work can be summarized as

- (a) welding torque reduces with decrease in APR (Fig. 2.29), and
- (b) the vertical force on workpiece is not a function of torque.

Since, the welding torque is a function of the frictional resistance due to shear stresses ( $\tau_{\text{shear}}$ ) generated within the workpiece, this lack of dependence of torque on vertical force suggests that Coulomb's law of friction is not effective during FSW. The trend of torque reaching a uniform value with a decreasing APR implies that the constant shear model of friction may in fact be more suitable. In fact, ALE simulations by Schmidt and Hattel (2005) also suggests that except for the plunge period, plastic deformation contributes substantially to the total heat generation indicating a sticking friction during FSW.

Another significant feature is the correlation between vertical and horizontal forces with the metallurgical band/onion ring formation during FSW (Yan et al. 2007). Figure 2.30 shows the variation in rotation speed, vertical and horizontal forces, displacement and traverse velocity in FSW (without and with welding) in details. Owing to the very nature of the equipment control used in FSW, an intrinsic periodicity in rotation rate, welding speed, and displacement ( $D_x$ ) is observed even without actual welding (Fig. 2.30a). However as expected, no cyclic variation in forces  $F_x$  and  $F_z$  (they occur in response to the interaction between tool with workpiece) are observed. The periodicity in the welding speed and displacement of the FSW tool (during free rotation without welding) is identical to the average angular velocity of the tool (e.g. if the tool is rotating at an average 300 rpm, the observed periodicity is 5 cycles/s (=300 rotations/60 s)). The angular velocity of tool itself was however found to be cyclic (e.g. if the average rotation is 300 rpm, the rotation rate itself varying sinusoidally over an upper and lower limit) with a unique periodicity characteristic of the FSW machine used and depends on its electronic controls. It is to be noted here that in some FSW equipment the welding speed and displacement during welding is measured by tracking the movement of workpiece. In such equipment no such periodicity in welding speed and displacement is expected. In Fig. 2.30b the variation in welding speed, displacement, and forces (vertical/horizontal) when actual welding process is carried out are shown. In this instance, unlike in the free rotation state, the horizontal and vertical forces (in addition to welding velocity) are observed to vary in an approximately sinusoidal fashion with a frequency equal to the average angular speed of tool rotation. The tool displacement was however observed to be unaffected by the welding. Further, this periodic variation in forces and welding velocity were independent of the extent of tool run-out although with increased tool run-out the mean value of horizontal force was found to decrease. The most interesting aspect of these findings is that the frequency of periodic variation in forces and welding velocity is identical to the frequency of occurrence of metallurgical banding (i.e. onion ring) formed during the welding (Fig. 2.31). In fact, this leads one to believe that periodicity of the forces in FSW is intrinsic to the material process and metallurgical banding is an intrinsic character of the welding process itself.

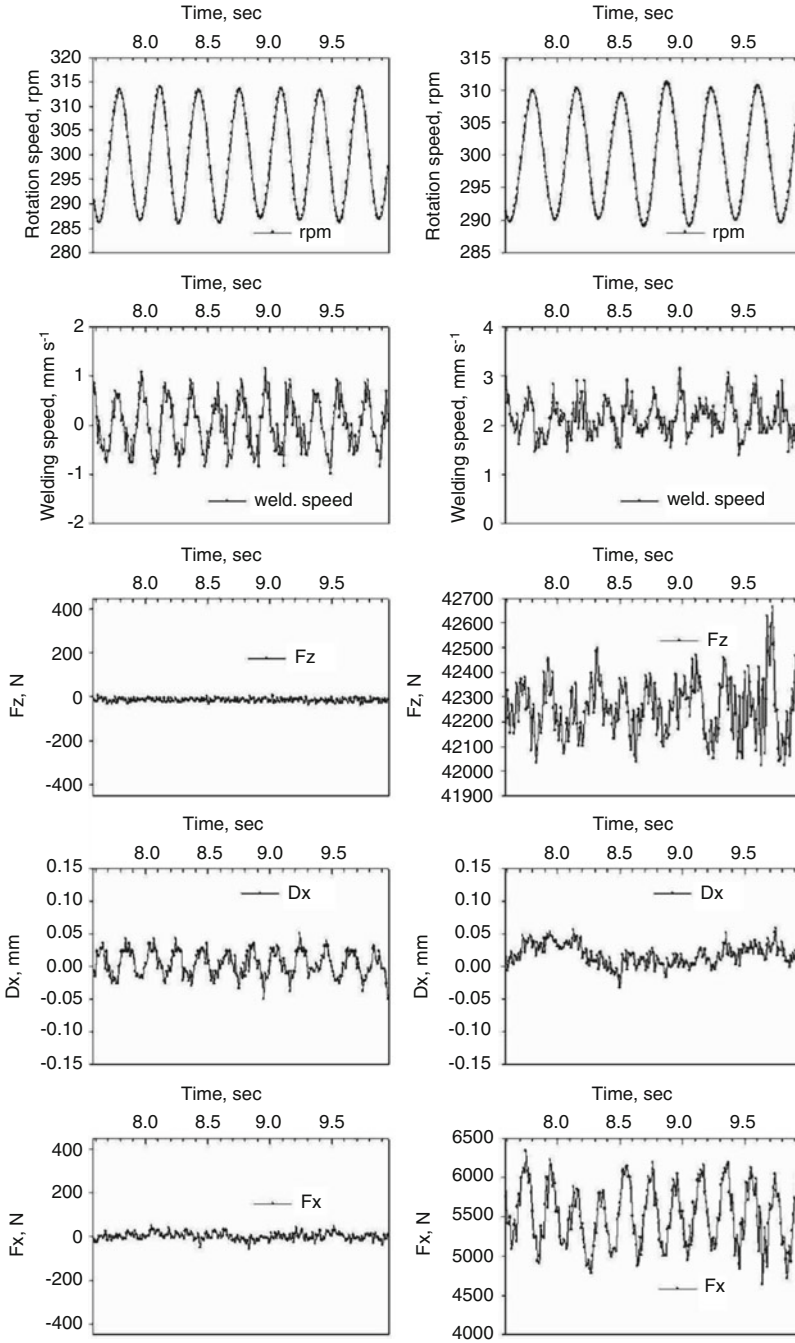
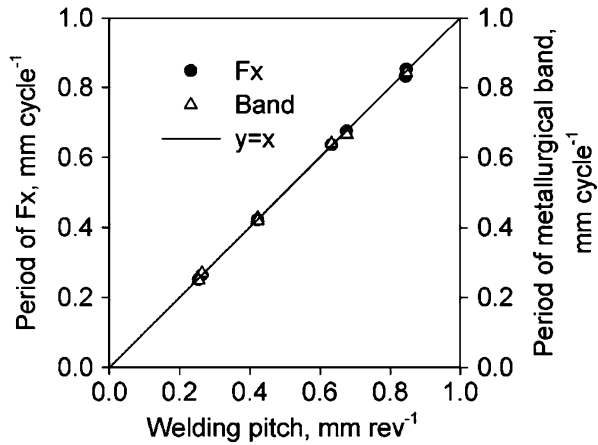


**Fig. 2.30** The variation in rotation speed, tool displacement, welding velocity and forces (*vertical and horizontal*) during (a) free rotation of tool and (b) during welding (Yan et al. 2007, reprinted with permission from Maney Publishing)

**Fig. 2.31** The correlation between the frequency of horizontal force cycle and metallurgical band cycle for different APR values during FSW (Yan et al. 2007, reprinted with permission from Maney Publishing)



**Box 2.8    Origin of Tool Run-Out**

The main contributor to the tool run-out is misalignment between spindle and tool holder. The eccentricity between the tool and spindle axes leads to run-out. A schematic illustrating various sources leading to tool run-out is shown in Fig. 2.32.

The diagram consists of four sub-figures labeled a, b, c, and d. Sub-figure (a) shows two concentric circles representing the spindle and tool axes, with labels 'Center of the Spindle axis' and 'Center of the tool axis' indicating a horizontal offset. Sub-figure (b) shows a cross-section of a tool with labels 'Center of the shoulder axis' and 'Center of the tool pin axis' indicating an offset between the shoulder and pin centers. Sub-figure (c) shows a circular cross-section with a dashed line for the spindle axis and a solid line for the tool axis, which are not parallel, causing the tool to wobble. Sub-figure (d) shows a tool pin being bent by a force F, with a curved arrow indicating the direction of the force.

**Fig. 2.32** The different sources of tool run-out in friction stir weld (a) shift between spindle and tool axis, (b) shift between the center of tool pin and shoulder, (c) non-parallel spindle and tool axis resulting in wobbling, (d) Pin bending (possible in tools with long pin)

## 2.5 Material Behavior and Constitutive Equations

Understanding the stress-strain relationship of a metal (i.e. the constitutive equation) during FSW is critical to have an insight into the process. The challenge partly stems from the fact that the temperature, strain and strain rate conditions in FSW vary at different positions of the weld. Consequently, the flow stress at different positions varies rendering a constant flow stress approach inadequate. Nevertheless, the customary approach is to model the material using constitutive equations where the material flow behavior is modeled either on a physical or on an empirical basis. Considering the physical approach first: modeling the behavior primarily involves an expression of deformation on the basis of dislocation movements (even though other physical effects like twinning or phase transformations can be involved depending on the material). The strain rate because of dislocation passage through a single crystal can be expressed as,

$$\dot{\gamma} = b\rho\bar{v}.$$

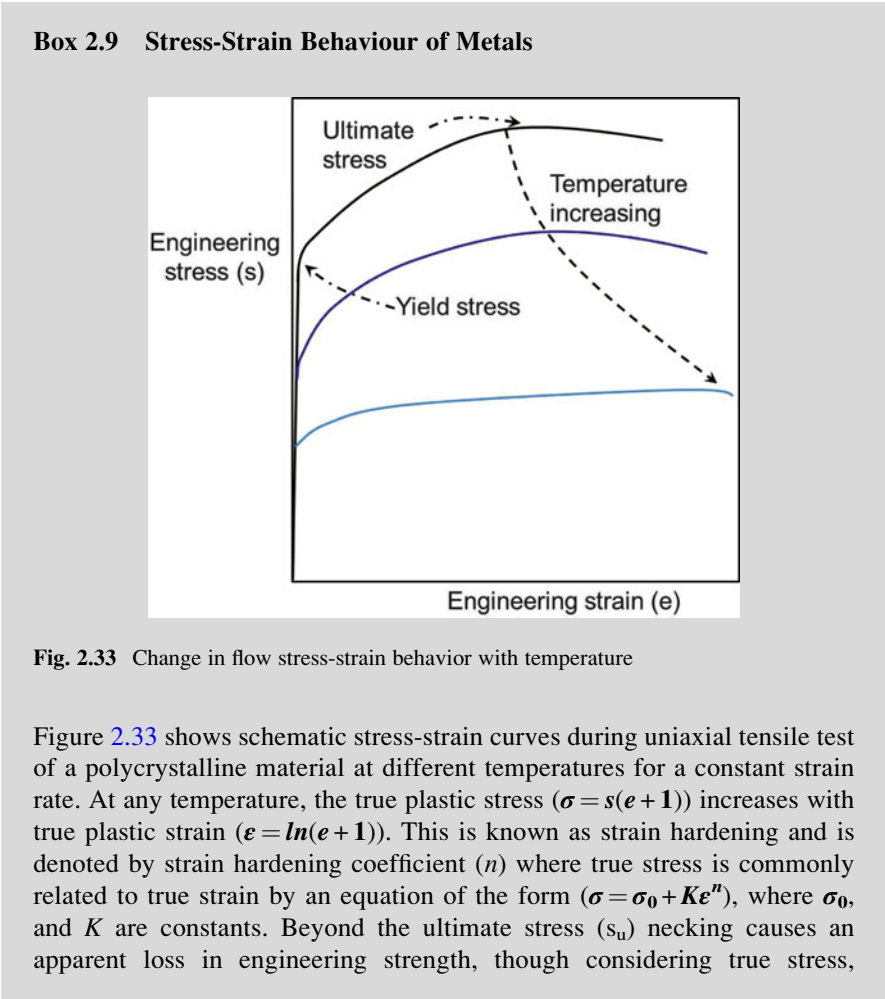
In the above equation deduced by Orowan,  $\dot{\gamma}$  is the shear strain rate,  $b$  is the Burger's vector of dislocation,  $\rho$  is the dislocation density and  $\bar{v}$  is the average dislocation velocity. For a given strain (i.e. constant dislocation density) the strain rate is, therefore, dependent on the dislocation velocity which itself depends on the microstructure, temperature and stress, and can be expressed as (Gilman 1969),

$$v = v_s^* \left(1 - e^{-\tau/s}\right) + v_d^* e^{-D/\tau}$$

where  $v_s^*$  and  $v_d^*$  are limiting velocities,  $s$  is the coupling stress,  $D$  is called the characteristic drag address and  $\tau$  is the applied shear stress. The extension of these effects to a polycrystalline material (as is the case for practical welding) requires a consideration for all individual slip systems in the crystals and incorporating the effect of their mutual interactions thereof. The problem however is non-trivial since dislocations are non-equilibrium structures and mechanical deformation is essentially an irreversible process, i.e. path dependent function. Thus, for a given dislocation density, the mobile dislocation velocity depends on the dislocation drag effects which is influenced by the immobile dislocation arrangements governed by the prior deformation history. This effect of deformation history becomes increasingly relevant at high strains and strain rates used in friction stir processes. Consequently, the use of physical based constitutive equations is rare and empirical approaches are more common. In Table 2.4 some examples of the commonly used constitutive equations in FSW are summarized. The correctness of these constitutive models is however determined by the accuracy and suitability of the material constants used for the particular applications. In the next part of this section we briefly discuss one of the common methods used to determine the empirical based constitutive equations.

**Table 2.4** Examples of different constitutive material behaviors adapted for FSW modeling.

Equation name (ref)	Equation form
Hansel-Spittel (Guerdoux and Fourment 2009)	$\bar{\sigma} = \sigma_f = K(T)(\sqrt{3}\dot{\bar{\epsilon}})^{m(T)}$
Johnson-Cook (Schmidt and Hattel 2005)	$\sigma_y = (A + B \bar{\epsilon}^{pl} ^n) \left( 1 + C \ln \frac{\dot{\bar{\epsilon}}^{pl}}{\dot{\epsilon}_0} \right) \left( 1 - \left( \frac{T - T_{ref}}{T_{melt} - T_{ref}} \right)^m \right)$
Sheppard and Wright (Nandan et al. 2006, Cho et al. 2013, Hamilton et al. (2013), Ulysse 2002)	$\sigma_e = \frac{1}{\alpha} \sinh^{-1} \left[ \left( \frac{Z}{A} \right)^{1/n} \right]$



(continued)

**Box 2.9** (continued)

material still strain hardens or reaches a saturation level. At a given temperature, change in the test strain rate again modifies the stress-strain behavior. This effect of strain rate on stress is known as the strain rate sensitivity ( $m$ ). The relation between true stress and true strain rate ( $\dot{\epsilon}$ ) at constant strain and temperature is generally expressed as ( $\sigma = C\dot{\epsilon}^m$ ), where  $C$  is a material constant. The effect of temperature ( $T$ ) on true stress at constant strain and strain rate is again given as ( $\sigma = C_1 \exp Q/RT$ ), where  $Q$  is the activation energy for plastic flow and  $C_1$  is the material constant. The equations describing the effect of strain, strain rate and temperature on stress can be further combined to give a general equation (see for example the Johnson-Cook equation). The strain rates for uniaxial tensile tests are in the range of  $0.00001$ – $0.1 \text{ s}^{-1}$  and are commonly known as quasi-static tests. Such quasi-static tests do not apply to FSW since the magnitudes of strain/strain rates are much lower.

### 2.5.1 Determination of Constitutive Equations at High Strain Rates

As indicated earlier, the commonly used quasi-static tensile testing methods are unsuitable for higher strain rate testing. This is due to the inertial effects of the test crosshead which causes difficulty in measuring the actual stress and strain conditions. Consequently, measuring the deformation behavior at high strain rates requires specialized testing conditions. The commonly used techniques include (Field et al. 2004),

- (a) drop-weight testing,
- (b) split-Hopkinson pressure bars or Kolsky bar, and
- (c) plate impact.

Of these, split-Hopkinson pressure bar is the most versatile and widely used technique (Fig. 2.34). This method was originally devised for compressive loading conditions (Hopkinson 1914) and has since then been adapted to tensile and torsional conditions also (Harding et al. 1960; Duffy et al. 1971).

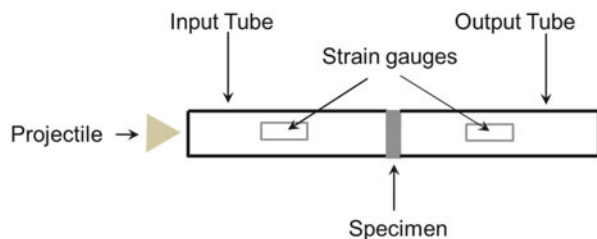


**Fig. 2.34** Schematic representation of a split-Hopkinson bar setup



The original version of this method comprises of two solid bars (called input and output bar) where a specimen is placed between the two such that they are in mechanical contact with each other. A projectile at high velocity is fired towards the specimen through the input bar, which on impact creates a compressive uniaxial incident stress wave. Part of this incident stress wave is reflected back from the specimen through the input bar, while the remaining part is transmitted through the output bar. In fact, both the input and output bars are designed in such a way that the reflected/transmitted stress waves are below their elastic deformation limits. The elastic strain (from embedded strain gauges) caused by the transmitted/reflected stress waves are recorded against time in both the input ( $\epsilon_{refl}$ ) and output ( $\epsilon_{trans}$ ) bars. Using this information the stress ( $\sigma$ ) and the corresponding strain ( $\epsilon$ ) imposed on the specimen is obtained as follows,

$$\sigma(t) = \frac{AE\epsilon_{trans}|_t}{A_s}$$

$$\frac{\partial \epsilon}{\partial t} = \frac{2c_b\epsilon_{refl}|_t}{l_s}$$

where  $A$  is the cross-sectional area of the bar,  $A_s$  is the area of the specimen,  $E$  is the Young's modulus of the material,  $c_b$  is the longitudinal wave velocity in the input/output bar material and  $l_s$  is the specimen thickness at the time instant and  $\partial \epsilon / \partial t$  is the specimen strain rate. The stress-strain diagram is further obtained by integrating the strain with time for the corresponding stress. Variations of this technique are used to measure the stress-strain behavior of material at various temperatures under different loading conditions. The data thus obtained are regressed to obtain the material constants for the selected constitutive equation.

## 2.6 Forces Around the Pin and Shoulder

As we wrap up this chapter, a simple schematic of forces around the pin are shown in Fig. 2.35 along with identification of various quadrants. This nomenclature is used in future chapters to discuss aspects around the pin or in the stir zone. The shear force from the pin surface is always tangential and in this figure marked as  $\tau_s$ . The shear force visualization is easier and this force is responsible shear layer formation. For a cylindrical pin without any features, this force engages with the material around the pin uniformly. The normal force exerted by the pin in the direction of travel is shown as  $\sigma_{pt}$ . The four quadrants are: Quadrant I-leading-advancing quadrant, Quadrant II-leading-retreating quadrant, Quadrant III-trailing-retreating quadrant and Quadrant IV-trailing-advancing quadrant. This figure can be used to discuss the influence of local forces on the material flow, friction coefficient at tool/workpiece interface, and defect formation.

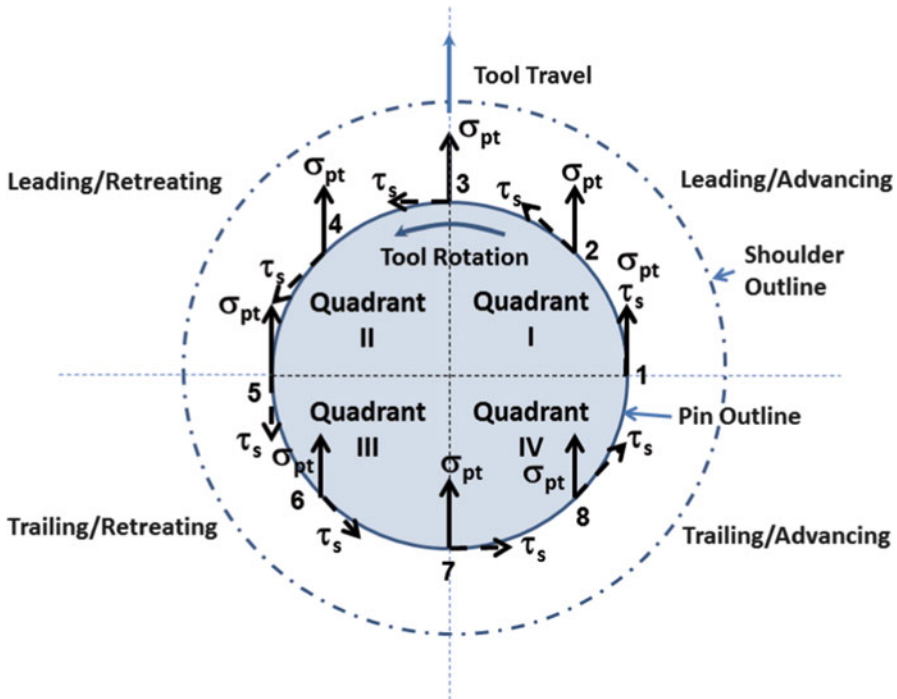


**Fig. 2.35** Forces around the pin during friction stir process. The pin cross-section is divided into four quadrants to facilitate discussion of interaction of pin with stir zone material around it

On the leading side, the  $\sigma_{pt}$  force pushes the material to the pin surface and the coupling will enhance the component of pressure dependent friction coefficient. On the other hand, the pin surface  $\sigma_{pt}$  forces on the trailing side exert no pressure on the material flowing behind. This lowers the engagement of flowing workpiece material with the pin surface. This not only would reduce the friction coefficient, but lead to lack of consolidation behind the pin. Although tool design and process parameters are discussed later, for initial concepts let us quickly consider two aspects. First, what happens to these forces if the pin shape is changed from cylindrical to conical. The  $\sigma_{pt}$  forces for a conical surface will have resolved downward component that was missing for the cylindrical pin surface. This will introduce a vertical or downward flow component that helps in enhanced material flow and consolidation. As discussed later in Chap. 4, lack of fill defects form near the bottom of pin between points 8 and 1 on the trailing/advancing side. Second, let us consider tool tilt which is often used to enhanced consolidation behind the tool. Again, a downward force component of  $\sigma_{pt}$  force on the trailing side can be visualized because of the tool tilt.

A more complex aspect is the influence of these forces on material flow. Let us take the pin surface region between points 1 and 2 (referred as 1–2), and compare it with region between points 2 and 3. At point 1, the  $\sigma_{pt}$  force does not have any normal component to the pin surface, and is aligned with the rotational shear

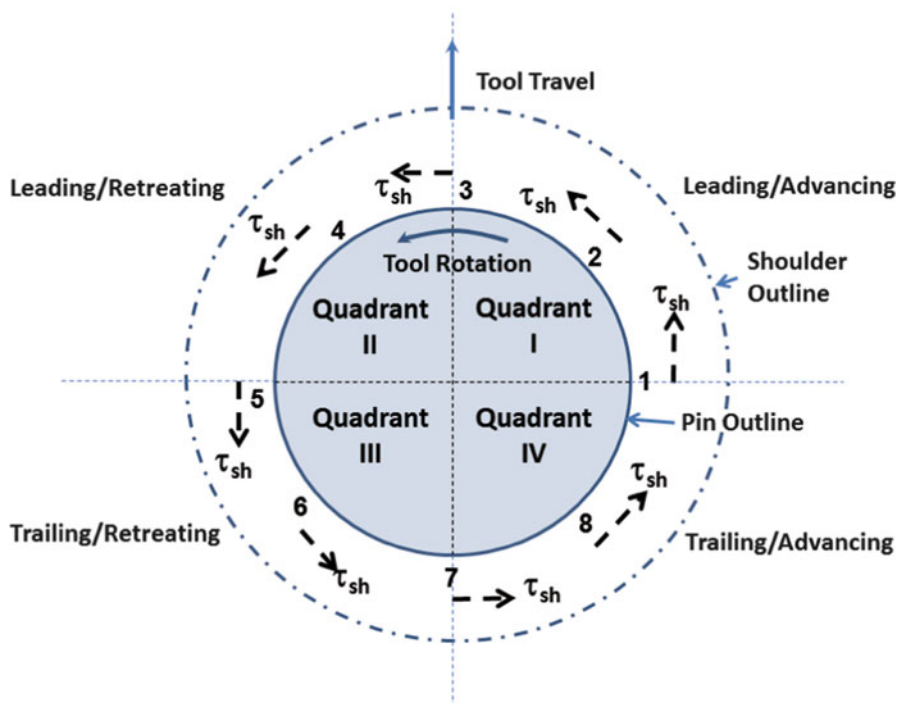


Fig. 2.36 Shoulder shear forces around the tool

component. Both force components oppose flow of material from the advancing side. In 1–2 region, the  $\sigma_{pt}$  force will have a resolved normal component to pin surface and resolved parallel component to pin surface. The pin surface normal component will try to displace the material towards the advancing side. Without going into any details in this chapter, some observations of faying surface hook formation and the length of feature line can be treated as indirect evidence of some material flow on the advancing side. But this gets complicated because of tool run-out and interpretation becomes more challenging. Figure 2.36 shows shear force vectors associated with shoulder. An interesting aspect is that shoulder induced flow in region 4–5–6 leads to change in the top surface shape of the nugget. For thin sheets, the shoulder influenced material flow can dominate the pin surface related flow. Examples of nugget shape are included in the next chapter.

## References

- C.D. Allen, J.A. Arbegast, Evaluation of friction stir spot welds in aluminum alloys. Paper 2005-01-1252, 2005 SAE World Congress, Society of Automotive Engineers, Detroit, MI, 2005
- W.J. Arbegast, A flow-partitioned deformation zone model for defect formation during friction stir welding. *Scripta Mater.* **58**, 372–376 (2008)

- A. Askari, S. Silling, B. London, M. Mahoney, Modeling and analysis of friction stir welding processes, in *Friction Stir Welding and Processing*, ed. by K.V. Jata, M.W. Mahoney, R.S. Mishra, S.L. Semiatin, D.P. Field (Warrendale, PA, TMS, 2001)
- H.J. Aval, S. Serajzadeh, A.H. Kokabi, Evolution of microstructures and mechanical properties in similar and dissimilar friction stir welding of AA5086 and AA6061. *Mater. Sci. Eng. A* **528**, 8071–8083 (2011)
- T. Belytchko, D.P. Flanagan, J.M. Kennedy, Finite element methods with user controlled mesh for fluid structure interaction. *Comput. Methods Appl. Mech. Eng.* **33**, 669–688 (1982)
- B. Bhushan, *Introduction to Tribology* (John Wiley and Sons, New York, NY, 2002)
- R.B. Bird, W.E. Stewart, E.N. Lightfoot, *Transport Phenomena*, 2nd edn. (John Wiley and Sons, New York, NY, 2007)
- F.P. Bowden, D. Tabor, *Friction—An Introduction to Tribology* (Doubleday and Company, Garden City, NY, 1973). Reprinted Krieger Publishing Co., Malabar, FL (1982)
- G. Buffa, J. Hua, R. Shivpuri, L. Fratini, A continuum based fem model for friction stir welding—model development. *Mater. Sci. Eng. A* **419**, 389–396 (2006a)
- G. Buffa, J. Hua, R. Shivpuri, L. Fratini, Design of the friction stir welding tool using the continuum based FEM model. *Mater. Sci. Eng. A* **419**, 381–388 (2006b)
- C.I. Chang, C.J. Lee, J.C. Huang, Relationship between grain size and Zener-Holloman parameter during friction stir processing in AZ31 Mg alloys. *Scripta Mater.* **51**, 509–514 (2004)
- Y.J. Chao, X. Qi, Thermal and thermo-mechanical modeling of friction stir welding of aluminum alloy 6061-T6. *J. Mater. Process. Manuf. Sci.* **7**, 215–233 (1998)
- Z.W. Chen, S. Cui, Strain and strain rate during friction stir welding/processing of Al-7 Si-0.3 Mg alloy. *IOP Conf. Ser. Mater. Sci. Eng.* **4**, 012026 (2009)
- H. Cho, S. Hong, J. Roh, H. Choi, S.H. Kang, R.J. Steel, H.N. Han, Three-dimensional numerical and experimental investigation on friction stir welding processes of ferritic stainless steel. *Acta Mater.* **61**, 2649–2661 (2013)
- P. Colegrove, M. Painter, D. Graham, T. Miller, 3-Dimensional flow and thermal modeling of the friction stir welding process, in *Proceedings of Second International Symposium on Friction Stir Welding*, June 2000
- K. Colligan, Material flow behaviour during friction stir welding of aluminum. *Welding J. Research Supplement*, 229s–237s (1999)
- K.J. Colligan, R.S. Mishra, A conceptual model for the process variables related to heat generation in friction stir welding of aluminum. *Scripta Mater.* **58**, 327–331 (2008)
- P.S. De, N. Kumar, J.Q. Su, R.S. Mishra, Fundamentals of friction stir welding. *ASM Handbook, Welding Fundamentals and Processes*, vol. 6A (2011)
- G.E. Dieter, *Mechanical Metallurgy*, 3rd edn. (McGraw-Hill Co., Boston, MA, 1986)
- J. Duffy, J.D. Campbell, R.H. Hawley, On the use of a torsional split Hopkinson bar to study rate effects in 1100-0 aluminum. *Trans. ASME J. Appl. Mech.* **38**, 83–91 (1971)
- D. Field, T. Nelson, Y. Hovanski, K. Jata, Heterogeneity of crystallographic texture in friction stir welds of aluminum. *Metall. Mater. Trans. A* **32**, 2869–2877 (2001)
- J.E. Field, S.M. Walley, W.G. Proud, H.T. Goldrein, C.R. Siviour, Review of experimental techniques for high rate deformation and shock studies. *Int. J. Impact Eng.* **30**, 725–775 (2004)
- V. Firouzdor, S. Kou, Al-to-Mg friction stir welding: effect of material position, travel speed and rotation speed. *Metall. Mater. Trans. A* **41**, 2914–2935 (2010)
- Ø. Frigaard, Ø. Grong, O. Midling, A process model for friction stir welding of age hardening aluminum alloys. *Metall. Mater. Trans. A* **32**, 1189–1200 (2001)
- A. Gerlich, G. Avramovic-Cingara, T.H. North, Stir zone microstructure and strain rate during friction stir spot welding. *Metall. Mater. Trans. A* **37**, 2773–2786 (2006)
- J.J. Gilman, *Micromechanics of Flow in Solids* (Mc-Graw-Hill, New York, NY, 1969), p. 179
- S. Guerdoux, L. Fourment, A 3D numerical simulation of different phases of friction stir welding. *Model. Simul. Mater. Sci. Eng.* **17**, 075001 (2009)
- M. Guerra, C. Schmidt, J.C. McClure, L.E. Murr, A.C. Nunes, Flow patterns during friction stir welding. *Mater. Charact.* **49**, 95–101 (2002)

- C. Hamilton, M. Kopyscianski, O. Senkov, S. Dymek, A coupled thermal/material flow model of friction stir welding applied to Sc-modified aluminium alloy. *Metall. Mater. Trans. A* **41**, 1730–1740 (2013)
- J. Harding, E.O. Wood, J.D. Campbell, Tensile testing of materials at impact rates of strain. *J. Mech. Eng. Sci.* **2**, 88–96 (1960)
- J. Hodowany, G. Ravichandran, A.J. Rosakis, P. Rosakis, Partition of plastic work into heat and stored energy in metals. *Exp. Mech.* **40**, 113–123 (2000)
- B. Hopkinson, A method of measuring the pressure produced in the detonation of high explosives or by the impact of bullets. *Philos. Trans. R. Soc. Lond. A* **213**, 437–456 (1914)
- T. Iwashita, Method and apparatus for joining, U.S. Patent 6,601,751, 2003
- D. Jacquin, B. de Meester, A. Simar, D. Deloison, F. Montheillet, C. Desrayaud, A simple Eulerian thermomechanical modeling of friction stir welding. *Journal of Materials Processing Technology* **211**, 57–65 (2011)
- K.V. Jata, S.L. Semiatin, Continuous dynamic recrystallization during friction stir welding of high strength aluminum alloys. *Scripta Mater.* **43**, 743–749 (2000)
- R. Kapoor, S. Nemat-Nasser, Determination of temperature rise during high strain-rate deformation. *Mech. Mater.* **27**, 1–12 (1998)
- M.Z.H. Khandkar, J.A. Khan, A.P. Reynolds, Prediction of temperature distribution and thermal history during friction stir welding: input torque model. *Sci. Technol. Weld. Join.* **8**, 165–174 (2003)
- M.Z.H. Khandkar, J.A. Khan, A.P. Reynolds, M.A. Sutton, Predicting residual thermal stresses in friction stir welded metals. *J. Mater. Process. Technol.* **174**, 195–203 (2006)
- G. Kohn, Y. Greenberg, I. Makover, A. Munitz, Laser-assisted friction stir welding. *Weld. Int.* **81** (2), 46–48 (2002)
- T.J. Lienert, W. Stellwag, L.R. Lehman, Comparison of heat inputs: friction stir welding vs. arc welding (2002), <http://174.122.108.74/conferences/abstracts/2002/011.pdf>
- B. London, M. Mahoney, W. Bingel, M. Calabrese, R.H. Bossi, D. Waldron, Material flow in friction stir welding monitored with Al-SiC and Al-W composite markers, TMS Annu Meet. 2003, p. 3–12.
- T. Long, W. Tang, A.P. Reynolds, Process response parameter relationships in Al alloy friction stir welds. *Sci. Technol. Weld. Join.* **12**, 311–317 (2007)
- M.W. Mahoney, C.G. Rhodes, J.G. Flintoff, R.A. Spurling, W.H. Bingel, Properties of friction stir-welded 7075 T651 aluminum. *Metall. Mater. Trans. A* **29**, 1955–1964 (1998)
- K. Masaki, Y.S. Sato, M. Maeda, H. Kokawa, Experimental estimation of strain rate during FSW of Al-alloy using plain strain compression. *Mater. Sci. Forum* **580–582**, 299–302 (2008a)
- K. Masaki, Y.S. Sato, M. Maeda, H. Kokawa, Experimental simulation of recrystallized microstructure in friction stir welded Al alloy using a plain-strain compression test. *Scripta Mater.* **58**, 355–360 (2008b)
- R.S. Mishra, Preface to the Viewpoint Set on friction stir processing. *Scripta Mater.* **58**, 325–326 (2008)
- S. Mukherjee, A.K. Ghosh, Flow visualization and estimation of strain and strain-rate during friction stir process. *Mater. Sci. Eng. A* **527**, 5130–5135 (2010)
- R. Nandan, G.G. Roy, T. Debroy, Numerical simulation of three-dimensional heat transfer and plastic flow during friction stir welding. *Metall. Mater. Trans. A* **32**, 1247–1259 (2006)
- A.C. Nunes Jr., Wiping metal transfer in friction stir welding, TMS Annu Meet. 2001, p. 235–248
- K. Okamoto, F. Hunt, S. Hirano, Development of friction stir welding technique and machine for aluminum sheet metal assembly. Paper 2005-01-1254, 2005 SAE World Congress, Society of Automotive Engineers, Detroit, MI, 2005
- S. Park, Y. Sato, H. Kokawa, Basal plane texture and flow pattern in friction stir weld of a magnesium alloy. *Metall. Mater. Trans. A Phys. Metall. Mater. Sci.* **34A**, 987–994 (2003)
- A.P. Reynolds, Microstructure development in aluminum alloy friction stir welds, in *Friction Stir Welding and Processing*, ed. by R.S. Mishra, M.W. Mahoney (ASM International, Materials Park, OH, 2007)

- A.P. Reynolds, Flow visualization and simulation in FSW. *Scripta Mater.* **58**, 338–342 (2008)
- J.R. Rule, J.C. Lippold, Physical simulation of friction stir welding and processing of Nickel-base alloys using hot torsion. *Metall. Mater. Trans. A* **44**, 3649–3663 (2013)
- M.J. Russell, H.R. Shercliff, Analytical modeling of microstructure development in friction stir welding, in *Proc. First Int. Symp. on Friction Stir Welding*, June 1999
- R. Sakano, K. Murakami, K. Yamashita, T. Hyoe, M. Fujimoto, M. Inuzuka, U. Nagano, H. Kashiki, Development of spot FSW robot system for automobile body members, in *Proceedings of the Third International Symposium of Friction Stir Welding*, Kobe, Japan, TWI, 27–28 Sept 2001
- Y. Sato, H. Kokawa, K. Ikeda, M. Enomoto, S. Jogan, T. Hashimoto, Microtexture in the friction-stir weld of an aluminum alloy. *Metall. Mater. Trans. A Phys. Metall. Mater. Sci.* **32**, 941–948 (2001)
- H. Schmidt, J. Hattel, J. Wert, An analytical model for the heat generation in friction stir welding. *Model. Simul. Mater. Sci. Eng.* **12**, 143–157 (2004)
- H. Schmidt, J. Hattel, A local model for the thermomechanical conditions in friction stir welding. *Model. Simul. Mater. Sci. Eng.* **13**, 77–93 (2005)
- H.N.B. Schmidt, T.L. Dickerson, J.H. Hattel, Material flow in butt friction stir welds in AA2024-T3. *Acta Mater.* **54**, 1199–1209 (2006)
- J.A. Schneider, A.C. Nunes Jr., Characterization of plastic flow and resulting microtextures in a friction stir weld. *Metall. Mater. Trans. B Process. Metall. Mater. Process. Sci.* **35**(2004), 777–783 (2004)
- T.U. Seidel, A.P. Reynolds, Visualization of the material flow in AA2195 friction-stir welds using a marker insert technique. *Metall. Mater. Trans. A* **32**, 2879–2884 (2001)
- A. Simar, Y. Brechet, B. de Meester, A. Denquin, C. Gallais, T. Pardoen, Integrated modeling of friction stir welding of 6xxx series Al alloys: process, microstructure and properties. *Prog. Mater. Sci.* **57**, 95–183 (2012)
- P. Su, A. Gerlich, T.H. North, G.J. Bendzsak, Material flow during friction stir welding. *Sci. Technol. Weld. Join.* **11**, 61–71 (2006)
- P. Su, A. Gerlich, T.H. North, G.J. Bendzsak, Intermixing in dissimilar friction stir spot welds. *Metall. Mater. Trans. A* **38**, 584–595 (2007)
- M.A. Sutton, B. Yang, A.P. Reynolds, J. Yan, Banded microstructure in 2024-T351 and 2524-T351 aluminum friction stir welds: part II. Mechanical characterization. *Mater. Sci. Eng. A* **364**, 66–74 (2004)
- Y. Tozaki, Y. Uematsu, K. Tokaji, Effect of tool geometry on microstructure and static strength in friction stir spot welded aluminum alloys. *Int. J. Mach. Tool. Manufact.* **47**, 2230–2236 (2007)
- P. Ulysse, Three-dimensional modeling of the friction stir welding process. *Int. J. Machine Tools Manuf.* **42**, 1549–1557 (2002)
- J. van der Lugt, J. Huetnik, Thermo-mechanically coupled finite element analysis in metal forming processes. *Comput. Methods Appl. Mech. Eng.* **54**, 145–160 (1896)
- J.H. Yan, M.A. Sutton, A.P. Reynolds, Processing and banding in AA2524 and AA2024 friction stir welding. *Sci. Technol. Weld. Join.* **12**, 390–401 (2007)
- B. Yang, J. Yan, M.A. Sutton, A.P. Reynolds, Banded microstructure in AA2024-T351 and AA2524-T351 aluminum friction stir welds: part I. Metallurgical studies. *Mater. Sci. Eng. A* **364**, 55–65 (2004)
- Q. Yang, S. Mironov, Y.S. Sato, K. Okamoto, Material flow during friction stir spot welding. *Mater. Sci. Eng. A* **527**, 4389–4398 (2010)
- O.C. Zienkiewicz, R.L. Taylor, J.Z. Zhu, *The Finite Element Method: Its Basis and Fundamentals*, 6th edn. (Butterworth Heinemann, Oxford, 2005)

Friction Stir Welding and Processing

Science and Engineering

Mishra, R.; De, P.S.; Kumar, N.

2014, XII, 338 p. 274 illus., 112 illus. in color.,

Hardcover

ISBN: 978-3-319-07042-1